JM PAPERS

# A hybrid artificial intelligence control of a turbulent jet: Reynolds number effect and scaling

**A.K. Perumal**[1,2,‡], **Z. Wu**[1,‡], **D.W. Fan**[1] **and Y. Zhou**[1,†]

[1]Center for Turbulence Control, Harbin Institute of Technology (Shenzhen), 518055 Shenzhen, PR China

[2]Jetacoustics and flow-control laboratory, Department of Aerospace Engineering, Indian Institute of Technology Kanpur, Kanpur 208016, India

This work aims to investigate experimentally the effect of the Reynolds number *Re,* based on the nozzle diameter *D*, on jet mixing manipulation using an unsteady radial minijet. A novel artificial intelligence (AI) control system has been developed to manipulate the jet over $Re = 5800$–$40\,000$. The system may optimize simultaneously the control law and a time-independent parameter, which dictate the actuation ON/OFF states and amplitude, respectively. The control parameters include the mass flow rate, excitation frequency and diameter ratios ($C_m$, $f_e/f_0$ and $d/D$) of the minijet to the main jet as well as the duty cycle ($\alpha$) of minijet injection. Jet mixing is quantified using $K_e$ and $K_0$, where $K$ is the decay rate of the jet centreline mean velocity, and subscripts $e$ and $0$ denote the manipulated and unforced jets, respectively. It has been found that the maximum $K_e$ achievable does not vary with *Re*. Scaling analysis of the huge volume of experimental data obtained from the AI system reveals that the relationship $K_e = g_1 (C_m, f_e/f_0, \alpha, d/D, Re, K_0)$ may be reduced to $K_e/K_0 = g_2 (\zeta)$, where $g_1$ and $g_2$ are different functions and the scaling factor $\zeta = (C_m/\alpha)(D/d)^{1-n}(1/Re)(f_e/f_{e,opt})^m$, $m$ and $1-n$ are the power indices, and subscript *opt* denotes the value at which $K_e$ is maximum. The scaling law is discussed in detail, along with the physical meanings of the dimensionless parameters $K_e/K_0$, $\zeta$, $(C_m/\alpha)(D/d)^{1-n}(1/Re)$ and $(f_e/f_{e,opt})^m$.

**Key words:** mixing enhancement, control theory, jets, machine learning

## 1. Introduction

As one of classical shear flows, the turbulent jet has been extensively studied in the past due to its vast range of applications in, e.g. aero and automobile engines, combustion, heat transfer and chemical reactors. Therefore, it is of both fundamental and practical significance to investigate how to manipulate a turbulent jet to achieve the desired

**942** A47-1

entrainment and mixing. Recent review articles by Reynolds *et al.* (2003), Knowles & Saddington (2006) and Henderson (2010) provide excellent compendiums for published papers on jet control.

Jet control can be passive and active. The former requires no power input, such as changing the geometric shape of nozzles (Mi & Nathan 2010), which is efficient and reliable. The latter, such as speaker- or plasma-based and fluidic control (e.g. Arbey & Williams 1984; Samimy *et al.* 2007; Yang & Zhou 2016), needs additional power input but may achieve more flexible and drastic flow modifications than the former (Perumal & Rathakrishnan 2022). Active methods are further divided into open- and closed-loop control, depending on whether sensor signals are used to drive actuation. Closed-loop control provides an opportunity to achieve a better performance than open-loop techniques. As such, various closed-loop control schemes have been developed for diversified applications, such as suppressing vortex shedding in wakes (Zhang, Cheng & Zhou 2004; Beaudoin *et al.* 2006; Pastoor *et al.* 2008), flow separation control (Gautier & Aider 2013) and jet mixing enhancement (Wu *et al.* 2016). Based on the time scale of the control loop and whether a model is required in a closed-loop system, Brunton & Noack (2015) classified the most used closed-loop systems into three categories: (i) stabilizing laminar flow, (ii) adaptive control of turbulence and (iii) model-free tuning of control laws. Category (i) is an in-time closed-loop control, usually based on white-box, grey-box or black-box model (Kim & Bewley 2007), where the 'in-time' means the time scale of the actuation response is much smaller than that of a natural flow. The white-box model, such as the direct solutions to Navier–Stokes equations, may resolve all flow features, while the grey-box model, e.g. the proper orthogonal decomposition model, captures merely limited flow features. Some successful applications of using a reduced-order model for the in-time control of fluid systems can be found in Noack, Morzynski & Tadmor (2011). The black-box model (e.g. transfer functions) only represents the input–output relationship. Category (ii) is based on the steady-state system response, and can be used only to optimize the given design of control laws in a slow manner as compared with the time scale of physical processes (Brunton & Noack 2015), e.g. extremum-seeking and slope-seeking control (Beaudoin *et al.* 2006). Category (iii) may realize rapid in-time control but needs a thorough understanding of the flow physics; examples include the proportional–integral–derivative (Zhang *et al.* 2004) and opposition control (Choi, Moin & Kim 1994) methods. However, a fluid system such as turbulent jet mixing enhancement involves a large range of temporal and spatial scales with complex nonlinear interactions. This makes model-based control difficult to implement. These challenges motivate the search for model-free control laws using machine learning methods, such as artificial neural networks and genetic programming (GP).

GP was developed in the 1990s and was rediscovered in fluid mechanics as machine learning control (MLC) by Gautier *et al.* (2015). Recently, the MLC method has been applied in numerous experiments and numerical simulations for control law optimization (Noack 2018). For example, MLC shows an extraordinary ability to find the optimal control law when deployed to enhance turbulent jet mixing using six independent unsteady minijets (Zhou *et al.* 2020). In the experimental systems of MLC developed so far, however, the discovered control law either regulates slowly, often less than 2 Hz, the actuation strength (Gautier *et al.* 2015) or determines rapidly only the ON/OFF states of actuators, with the actuation strength or amplitude and the Reynolds number *Re* fixed (e.g. Li *et al.* 2017; Wu *et al.* 2018*a*). Given varying flow conditions such as changing *Re*, the actuation strength may need to be optimized as well in order to obtain the best control performance. Then one issue naturally arises. Can we develop an MLC or artificial

intelligence (AI) control system that may optimize both actuation states and strength simultaneously? Furthermore, an AI control system may produce hundreds or thousands of control laws (e.g. Zhou *et al.* 2020) and accordingly a huge amount of data where all the control variables, along with the cost function or control goal, are physically connected. Can we extract an in-depth physical insight into the underlying control mechanism and inter-connection between the control variables based on a careful analysis of the data?

The effect of *Re* on an unforced jet has been investigated by e.g. Ricou & Spalding (1961), Panchapakesan & Lumley (1993), Hussein, Capp & George (1994) and Mi, Xu & Zhou (2013). These investigations unveiled that the centreline velocity, jet decay, ratio of mass entrainment to the mass flow rate at the jet exit and mean velocity profiles are independent of *Re* for $10\,000 \leq Re \leq 20\,000$. There have also been several studies on the *Re* effect of jet control. For example, Parekh, Leonard & Reynolds (1988) studied a jet controlled by an axial acoustic actuator at one end of the upstream plenum chamber and 4 equidistantly placed radial acoustic actuators around the nozzle exit with phases of 0°, 90°, 180° and 270° at *Re* from $10^4$ to $10^5$. The bifurcating jet could be produced at a frequency ratio between the axial and radial excitations of 2, and the excitation amplitude required to produce bifurcating jets was found to increase with *Re*. Wu, Wong & Zhou (2018*b*) manipulated a turbulent round jet based on single-frequency radial fluidic injection using a dual-input–single-output extremum-seeking technique. With the actuation frequency and mass flow rate ratio optimized simultaneously, the maximum jet entrainment/mixing rate was found to be unchanged from $Re = 5700$ to 13 300. The same conclusion was reached when this technique was further extended to three control parameters, with the duty cycle $\alpha$ of an unsteady minijet simultaneously optimized, by Fan *et al.* (2020). However, there is a lack of information on the dependence on *Re* of the inter-relationship between the jet entrainment or mixing rate and the control parameters. The possible important impact of *Re* on the control performance has yet to be thoroughly documented in the literature.

Unsteady fluidic injection may have a number of control parameters, including the mass flow rate, excitation frequency and diameter ratios, $C_m, f_e/f_0$ and $d/D$, of minijet to main jet as well as the duty cycle $\alpha$ of minijet injection, where $f_0$ is the preferred-mode frequency of an unforced main jet. Perumal & Zhou (2018) conducted an empirical scaling analysis on a jet manipulated by single unsteady minijet at $Re = 8000$. Their study reveals that the jet centreline mean velocity decay rate $K_e = f_1 (C_m, d/D, \alpha)$ may be reduced to $K_e = f_2 (\xi)$ and the scaling factor $\xi = (\sqrt{MR}/\alpha)(d/D)^n$, where $f_1$ and $f_2$ are different functions, $\sqrt{MR} = C_m(D/d)$ is physically the effective momentum ratio per pulse and $n$ is a function of $\alpha$. Here MR is the momentum ratio of the minijet to the main jet. However, *Re* and $f_e/f_0$ have not been considered in this scaling law. A variation in *Re* may influence jet mixing (e.g. New, Lim & Luo 2006; Mi *et al.* 2013) and hence the centreline mean velocity decay rate $K_0$ for an unforced jet. As such, under manipulation, $K_e$ may also depend on $K_0$ given a varying *Re*. One important question naturally arises: Can we find a physically meaningful scaling factor $\zeta$ so that $K_e = g_1 (C_m, f_e/f_0, \alpha, d/D, Re, K_0)$ may be reduced to $K_e = g_2 (\zeta)$? Such a scaling factor $\zeta$ is of great significance, and may be used to design unsteady fluidic injectors for full-scale practical applications (Wickersham 2007).

This work aims to address the issues raised above. An extended AI control system, termed a hybrid AI control system hereinafter, is developed to manipulate a turbulent jet based on a pulsed minijet, with a view to maximizing its mixing. The system is capable of searching simultaneously a near-optimal control law and a time-independent parameter in spite of a variation in *Re*. The *Re* effect on control performance and the optimal control parameters are investigated over $Re = 5800$–40 000, covering the regimes of $Re < Re_{cr}$ and $Re \geq Re_{cr}$ to document the effect of *Re* on jet mixing, where $Re_{cr}$ is the critical Reynolds
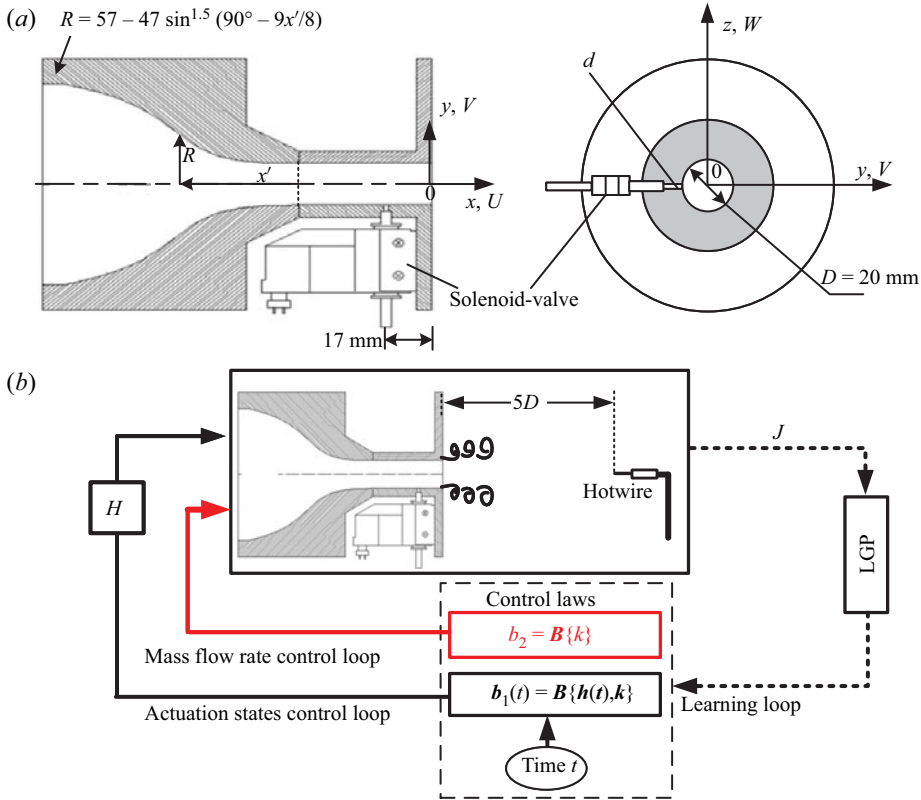
Figure 1. (*a*) Schematic of experimental set-up; (*b*) sketch of principle of the hybrid AI system.

number, $\sim$10 000, at which turbulent 'mixing transition' starts (Mi *et al.* 2013). A scaling analysis is then performed based on the massive data produced from the AI system. The manuscript is organized as follows. Section 2 describes the experimental set-up. Section 3 introduces the hybrid AI system. The *Re* effect on control performance is presented in § 4. A scaling law is extracted from experimental data in § 5, along with a detailed discussion of involved dimensionless parameters. This work is concluded in § 6.

## 2. Experimental details and unforced jet

### 2.1. *Jet facility and actuator system*

The jet rig to produce an axisymmetric main jet, along with the assembly to generate a pulsed minijet, is the same as used in Wu *et al.* (2018*a*) and is briefly introduced here. As shown in figure 1(*a*), the nozzle is extended with a 47 mm long smooth tube with the same inner diameter $D = 20$ mm as the nozzle exit. A radial pinhole of diameter $d$ is made 17 mm upstream of the main jet exit. Two pinhole diameters, i.e. 0.5 mm and 1.0 mm, are chosen, resulting in $d/D = 1/20$ and 1/40, respectively. Seven different Reynolds numbers $Re \equiv \bar{U}_j D/\nu$, varying from 5800 to 40 000, are examined, where $U_j$ is the velocity measured at the centre of the jet exit ($x^* = 0.05$), the overbar denotes time averaging and $\nu$ is the kinematic viscosity of air. In this paper, an asterisk superscript denotes normalization by $D$ or/and $\bar{U}_j$. The coordinate system ($x$, $y$, $z$) is defined in figure 1(*a*), with its origin at the centre of the jet exit.

The mass flow rate of the minijet through the pinhole is measured using a mass flow controller (FLOWMETHOD FL-802) with a measurement range of 0–7 l min$^{-1}$, whose experimental uncertainty is no more than 1 %. The duty cycle and frequency of the minijet injection are controlled using an electromagnetic valve that is operated on an ON/OFF mode with a maximum operating frequency of 500 Hz.

## 2.2. *Flow measurement and control instruments*

The instantaneous velocity in the jet is measured using a single hot-wire. The sensor is a 1 mm long tungsten wire of 5 µm diameter operated, at an overheat ratio of 1.8, on a constant temperature mode (Dantec Streamline). The hot-wire is mounted on a three-dimensional traverse system to measure the jet centreline velocities, $U_j$ and $U_{5D,0}$, at the jet exit and $5D$ downstream, respectively, without control and also $U_{5D,e}$ under control. The output signal is offset, amplified and filtered by a low-pass filter at a cutoff frequency of 500 Hz before being digitized at a sampling frequency $F_{RT}$ of 10 kHz. The hot-wire is calibrated at the jet exit using a Pitot tube and a micromanometer (Furness Controls FCO510). The experimental uncertainty in measured $\bar{U}_j$, $\bar{U}_{5D,e}$ or $\bar{U}_{5D,0}$ is estimated to be within 2 %.

The real-time control is implemented via a National Instrument PXI system, which consists of a chassis, a multi-function I/O Device (PXIe-6356) and a controller (PXIe-8821). A LabVIEW Real-Time module is used for digitizing the analogue signal and providing control commands for the mass flow controller and electromagnetic valve at a loop time of 100 µs ($F_{RT} = 10$ kHz). The same sampling rate is used for the velocity data acquisition and control command generation. As discussed in Wu et al ([2018a](#)), the available duty cycles $\alpha$ are determined by $F_{RT}$ and periodic excitation frequencies $f_e$. For instance, there are 48 possible $\alpha$ values available for use given $F_{RT} = 10$ kHz and $f_e = 200$ Hz.

## 2.3. *Unforced jet characteristics*

In the absence of control, $\bar{U}^*$ exhibits a 'top-hat' profile (figure 2a) and the corresponding root-mean-squared (r.m.s.) velocity $u_{rms}^*$ is less than 0.06 (figure 2b) at $Re = 20\ 000$. Both $\bar{U}^*$ and $u_{rms}^*$ collapse reasonably well with Mi *et al.*'s ([2013](#)) data at $Re = 20\ 100$. The displacement thickness $\delta$ and momentum thickness $\theta$ estimated from the velocity profile are 0.57 mm and 0.21 mm, respectively, at the nozzle exit for $Re = 8000$ (Perumal & Zhou [2021](#)), which are very close to their counterparts (0.56 mm and 0.24 mm) measured at approximately the same $Re$ (=8050) by Mi et al ([2013](#)). The shape factor $H = \delta/\theta$ is 2.71, slightly higher than the Blasius flat plate value ($H = 2.59$), suggesting that the boundary layer at the nozzle exit is close to laminar. With increasing $Re$, both $\delta$ and $\theta$ decrease, as noted by Mi *et al.* ([2013](#)), and $H$ drops to 2.49 and 2.41 for $Re = 13\ 300$ and 20 000, respectively, suggesting a turbulent boundary layer at the nozzle exit. The streamwise variations of $\bar{U}^*$ and $u_{rms}^*$ also agree with each other between the two studies (figure 2c,d).

The flow visualization images for an unforced jet at various $Re$ are presented in figure 3. At $Re = 5800$ and 8000 (figure 3a,b), the quasi-periodical ring vortices exhibit laminar features during the initial rollup process and then gradually transition to turbulence. Once $Re$ exceeds 10 000 (figure 3c,d), the vortices appear to be turbulent from the beginning and the jet spreads out more rapidly than $Re < 10\ 000$. This is also supported by the streamwise fluctuating velocity signals $U^*$ measured along the jet axis for the natural jet at $Re = 8000$–20 000 (figure 4). The flow is clearly laminar near the nozzle exit ($x^* \leq 3.0$) at $Re = 8000$ but displays random fluctuations, a feature of turbulence, starting from $Re = 10$
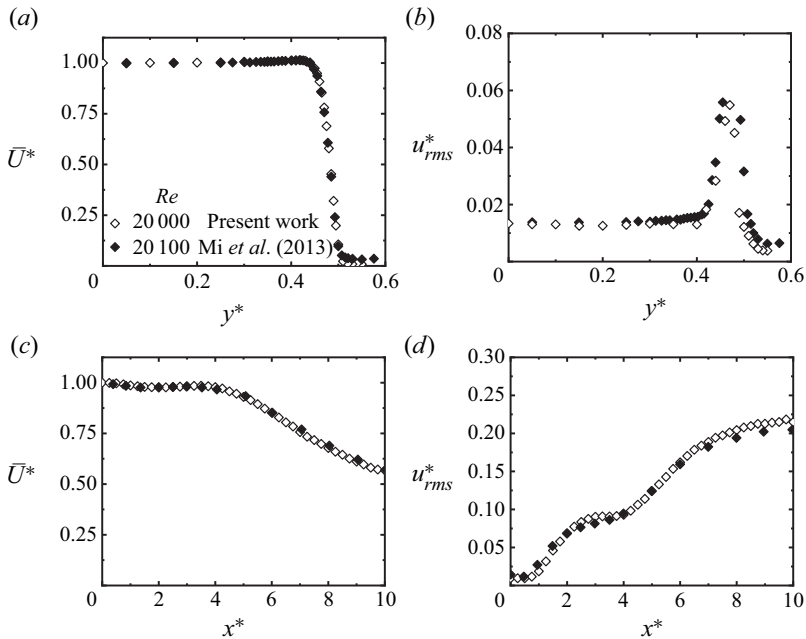
Figure 2. (*a,b*) Radial distributions of $\bar{U}^*$ and $u_{rms}^*$ measured at $x^* = 0.05$ in the (*x–y*) plane and (*c,d*) streamwise variations of centreline mean and r.m.s. velocities for $Re = 20\,000$. Mi *et al.* (2013) is included for comparison.
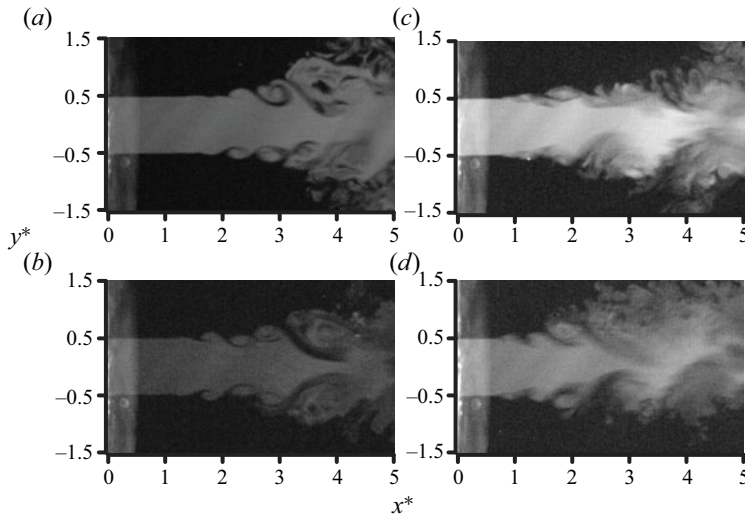


Figure 3. Flow visualization of unforced jet in the (*x–y*) plane for (*a*) $Re = 5800$, (*b*) 8000, (*c*) 10 600 and (*d*) 13 300.

600 and becoming more evident at $Re = 20\,000$. Mi *et al.*'s (2013) extensive hot-wire measurements over $Re = 4000$–20 000 indicated that the mean flow decay rate and spread vary with *Re* given $Re < 10\,000$ and tend to become *Re*-independent for $Re > 10\,000$. Furthermore, the small-scale turbulence properties, such as the mean dissipation rate of kinetic energy and the Kolmogorov and Taylor microscales, vary differently between the two *Re* ranges. It seems plausible from both the present and Mi *et al.*'s measurements
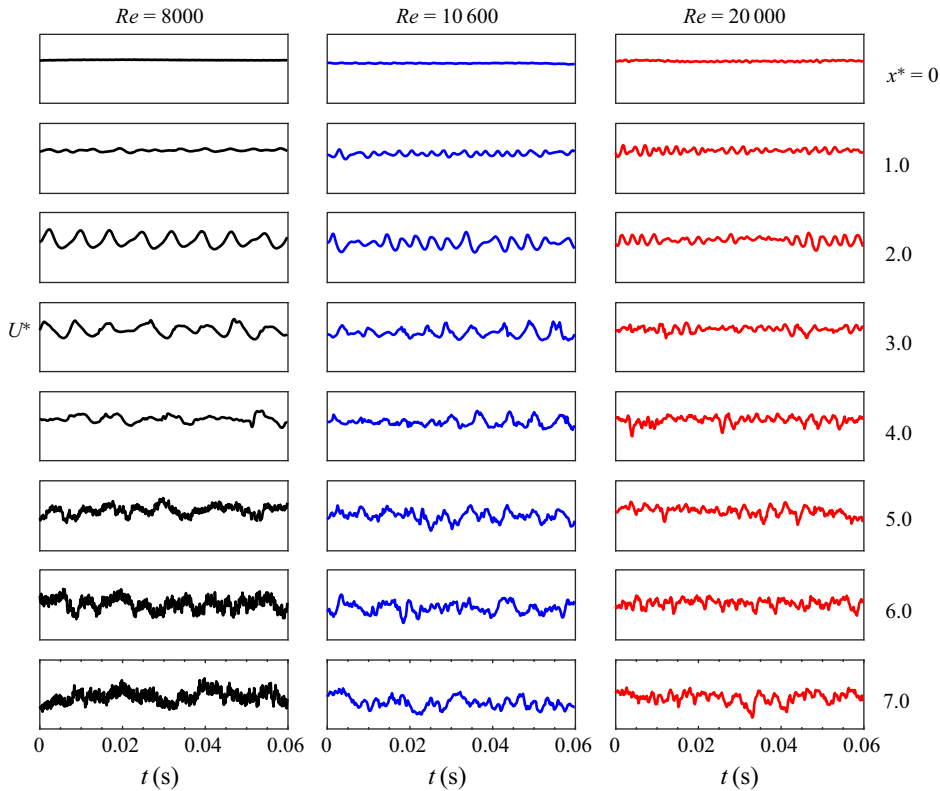
Figure 4. Typical signals of instantaneous streamwise $U^*$ measured along jet centreline ($y^*$ and $z^* = 0$) for the natural jet at $Re = 8000$–$20\,000$. The same scale is applied for all signals.

that $Re = 10\,000$ is a critical Reynolds number across which the jet turbulence behaves distinctly.

The power spectral density functions of streamwise velocity $U$ measured along the centreline for $x^* = 2$–$6$ show a pronounced peak at $f_0 = 100$–$680$ Hz for $Re = 5800$–$40\,000$, as shown by Fan *et al.* (2017) for $Re = 8000$–$16\,000$, suggesting the occurrence of the preferred-mode structures. The corresponding Strouhal number $St(\equiv f_0 D / \bar{U}_j)$ varies between 0.45 and 0.50, falling in the range of 0.24–0.64 for a natural jet (Crow & Champagne 1971). The unforced jet develops slowly at $x^* \leq 5$, and the $Re$-related variation of jet centreline mean velocity is small, within 2.5 %, for $4050 \leq Re \leq 20\,100$ (Mi *et al.* 2013).

## 2.4. *Evaluation of jet decay rate and mixing*

Following Zhou *et al.* (2012) and Perumal & Zhou (2018), the decay rate $K_e$ of the jet centreline mean velocity is used to evaluate jet entrainment rate, defined by

$$K_e = \frac{\bar{U}_j - \bar{U}_{5D,e}}{\bar{U}_j}, \tag{2.1}$$

where $\bar{U}_{5D}$ and $\bar{U}_j$ denote the jet centreline mean velocities at $x^* = 5$ and $x^* \approx 0$, respectively. This quantity may also provide a measure for the mixing efficacy of the jet based on the following considerations. Firstly, as documented by Fan *et al.* (2017), the
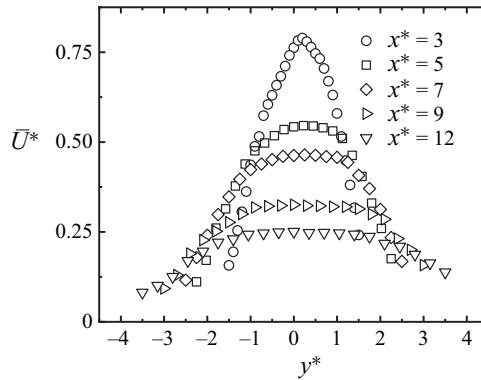
Figure 5. Normalized streamwise mean velocities measured along the $y$ axis at different axial locations for $C_m = 5.0\,\%$, $f_e/f_0 = 0.5$, $\alpha = 0.1$ and $d/D = 1/20$ at $Re = 13\,300$.

difference $\Delta K$ between the $K_e$ values with and without control reaches a maximum at $x^* \approx 5$ (their figure 7), that is, $K_e$ estimated based on the streamwise velocity measured at $x^* = 5$ is most sensitive to control. Secondly, $K_e$ is correlated with both the jet half-width and potential core length. Zhou *et al.* (2012) demonstrated that $K_e$ is related approximately linearly to an equivalent jet half-width $R_{eq} = [R_H R_V]^{1/2}$, where $R_H$ and $R_V$ are the jet half-widths in two orthogonal planes, that is, $K_e$ is directly connected to the entrainment rate of the manipulated jet. Furthermore, an increase in $K_e$ corresponds to a decrease in the potential core length of the jet (Perumal & Zhou 2018), implying that $K_e$ may provide a measure for jet mixing. Finally, this one-point criterion for jet mixing has also been used by other researchers (e.g. Breidenthal *et al.* 1985; Wickersham 2007). Breidenthal *et al.* (1985) used an aspirating probe to measure the concentration fluctuation $c$ of two mixing streams, i.e. a rectangular duct flow and a transverse jet, and noted that the decay rate of the r.m.s. value $c_{rms}$ of $c$ was almost linearly related to the momentum ratio of the transverse jet to the rectangular duct flow. This relationship persisted over $x^* = 1 \sim 10$ (see their figure 5). As such, they used the single decay rate of $c_{rms}$, measured at $x^* = 8.9$, to characterize the mixing of the two streams and argued that this decay rate provided a measure for the mixing efficacy of turbulence.

The main jet may deflect when manipulated asymmetrically using a single minijet. One question naturally arises as to whether the jet decay rate may be estimated correctly from the centreline mean velocities. Perumal & Zhou (2018) manipulated a round jet at $Re = 8000$ using a single minijet injection and presented the normalized mean velocity profiles in two orthogonal planes (see their figure 6) for the manipulated jet at $C_m = 1.0\,\%$, $f_e/f_0 = 0.5$, $\alpha = 0.1$ and $d/D = 1/20$. The manipulated jet exhibited a reasonable symmetry about the geometric centre ($y^* = 0$ or $z^* = 0$), showing a slight deviation in the location of the maximum velocity from this centre and causing an error of no more than $1\,\%$ in $K_e$. This deviation apparently depends on $C_m$ which is presently up to $5.0\,\%$. As such, figure 5 presents the normalized streamwise mean velocities measured along the injection direction ($y$ axis) at different axial locations for $C_m = 5.0\,\%$, $f_e/f_0 = 0.5$, $\alpha = 0.1$ and $d/D = 1/20$ ($Re = 13\,300$). Evidently, the difference between the maximum velocity and the velocity at the geometric centre is very small, resulting in an error of no more than $1\,\%$ in $K_e$ at $x^* = 3$. This difference diminishes with increasing $x^*$. It may be concluded that the effect of the jet defection, due to a single minijet injection, is negligibly small in the present experimental conditions. Note that this difference may grow appreciably for a quasi-steady control, i.e. at large $\alpha$ and $f_e/f_0$, when the jet column deflects away from the geometric centreline, producing an increased artificial mixing (Perumal & Zhou 2018).
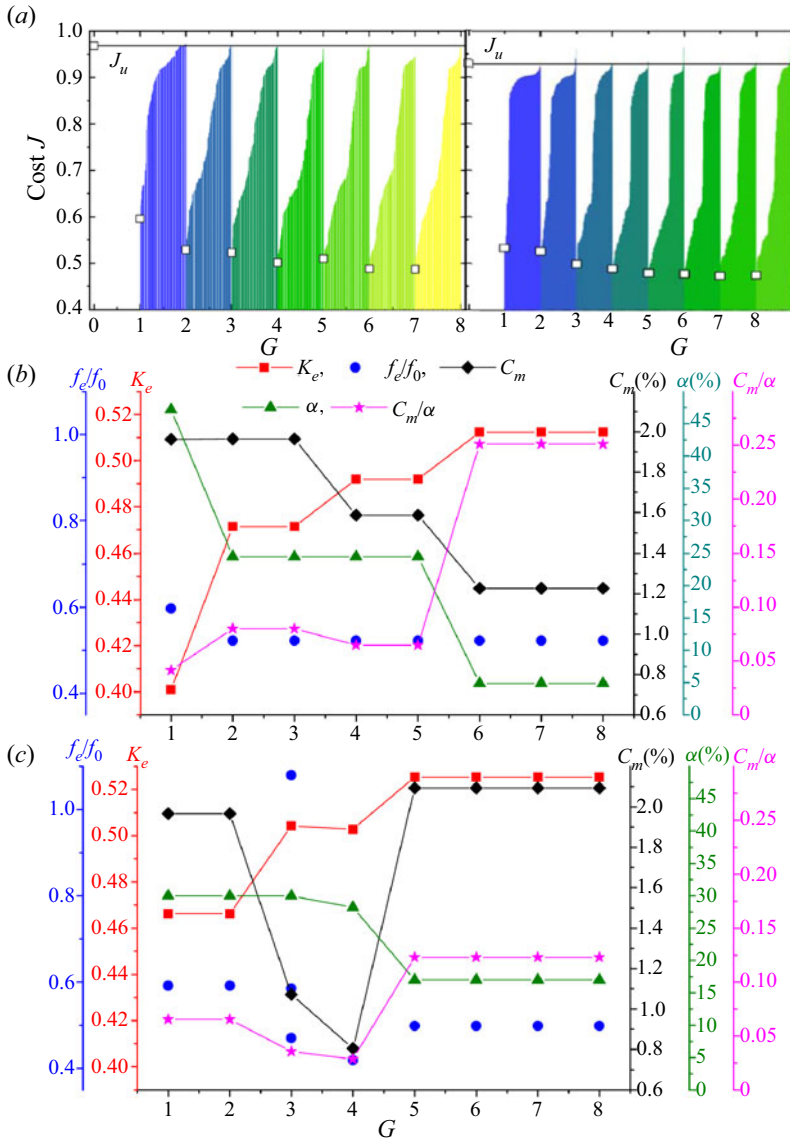
Figure 6. (*a*) Learning curves of AI control (left: $Re = 8000$; right: $Re = 20\,000$). Here, $J_u$ is the cost value corresponding to the benchmark of an unforced jet. The open square symbol denotes the best individual for each generation. (*b,c*) Evolution of the control parameters, associated with the best individual in each generation, and the corresponding $K_e$: (*b*) $Re = 8000$, (*c*) 20 000.

## 3. Controller design: hybrid AI system

Following our previous work (Wu *et al.* 2018*a*; Zhou *et al.* 2020), the cost function $J$ is defined as $\bar{U}_{5D,e}$ normalized with $\bar{U}_j$

$$ J = \frac{\bar{U}_{5D,e}}{\bar{U}_j} = 1 - K_e. \tag{3.1} $$

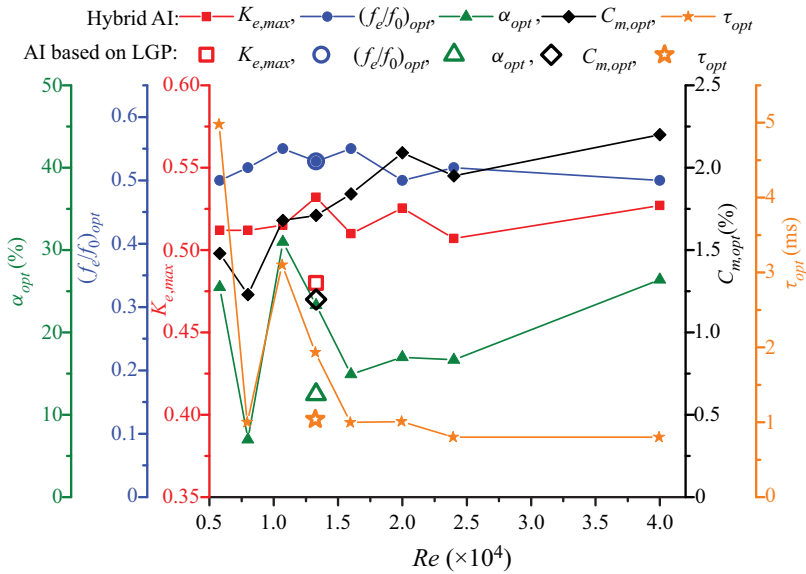Apparently, minimizing $J$ is equivalent to maximizing $K_e$.

Figure 7. The optimum control parameters obtained at different *Re* from AI control. The open symbols correspond to the data obtained at a fixed $C_m = 1.2\%$.

The major difference between the presently developed hybrid AI and previously reported AI/MLC systems (e.g. Parezanović *et al.* 2015; Li *et al.* 2017; Wu *et al.* 2018*a*; Zhou *et al.* 2020) is that the latter searches only for the control laws, while the former optimizes an independent control parameter ($C_m$), along with the control laws. The GP-based systems, developed by Wu *et al.* (2018*a*) and Zhou *et al.* (2020), may work on a multi-frequency forcing mode and/or a sensor-based feedback mode. The former, characterized by $\alpha$, $f_e$ and a number of distinct frequencies in the control law, is found to overwhelm the latter in performance. As such, only is the former presently examined, and the control law assumes following form:

$$b(t) = B(h(t), k), \tag{3.2}$$

where $B$ is a vector consisting of functions generating actuation commands, argument $k$ is a set of random constants and $h(t)$ is a set of input harmonic functions of time $t$, viz.

$$h(t) = [h_1 h_2 \ldots h_{11}]^T, \quad h_i = \cos(2\pi f_i t), \quad i = 1, 2, \ldots, 11. \tag{3.3}$$

The choice of eleven harmonic functions follows Wu *et al.* (2018*a*). Here, $B$ can be linear, quadratic or any other nonlinear function, and a large range of frequencies can be generated in the control signals. The control law in previously reported AI systems yields in general a time-variant binary signal for multi-frequency forcing (e.g. Li *et al.* 2017; Wu *et al.* 2018*a*; Zhou *et al.* 2020), with a fixed actuation strength ($C_m$). Yet, it may be desirable to optimize, other than the control law, a time-independent parameter, say $C_m$, to maintain the best control performance with varying flow conditions, such as *Re*. Note that a genetic algorithm (GA) works only on a population of constants and is thus suited for optimizing the parameters, such as $C_m$, of a preset open-loop control law (e.g. Qiao *et al.* 2021; Yu *et al.* 2022), while GP works on a population of hierarchical computer programs of varying sizes and shapes (Koza 1990), which may cover the open-loop control laws of different forms (such as single- or multi-frequency forcing laws) or the function of real-time feedback/feedforward sensor signals in a closed-loop system. As such, the latter

is characterized by a larger search space than GA and often outperforms the former, as illustrated by Li *et al.* (2017) for reducing the drag of a car model. We may modify GP by replacing the time-dependent functions with time-independent functions in order to optimize the time-independent parameters, as a GA does. Combining this modified GP with a 'conventional' GP forms a so-called hybrid AI system, which may optimize not only the parameters of a preset open-loop control law but also the control laws, be they open or closed loop.

Figure 1(*b*) presents a schematic for the hybrid AI control, where the control law $b(t)$ contains two independent actuation commands, i.e. time-dependent binary signal $b_1(t)$ and time-independent parameter $b_2$, viz.

$$b(t) = [b_1(t), b_2]^T = [\mathbf{B}(h(t), k), B(k)]^T. \tag{3.4}$$

Control law $b_1(t)$ is in the form of a Heaviside function $H$ to drive the electro-magnetic valve, producing and varying multiple excitation frequencies ($f_e$) and duty cycle ($\alpha$), while $b_2$ is a function of 17 random constants ranging from $-1$ to 1, and dictates $C_m$. The ensuing actuation produces a pulsed minijet whose maximum velocity is proportional to $C_m$ and $1/\alpha$ before the minijet is choked (Perumal & Zhou 2018).

The optimization process is the same as in Wu *et al.* (2018*a*) and Zhou *et al.* (2020). Briefly, linear genetic programming (LGP) acts as a regression solver to search for a law in the form of (3.4) that minimizes the cost function $J$ involving four major components: (i) creating a population of $N_i = 100$ control laws, (ii) evaluating the performance of each control law, (iii) checking whether the minimum $J$ is converged and (iv) evolving to the next generation where 100 new control laws are generated based on the performance of the previous generation. Please refer to Li *et al.* (2017) for a detailed description of LGP.

## 4. Reynolds number effect on control performance

The robustness of the hybrid AI control is examined by performing experiments with *Re* varying from 5800 to 40 000. Figure 6(*a*) shows the learning curves of the AI control at $Re = 8000$ and 20 000, where a colour bar consists of the costs $J$ corresponding to the 100 control laws of each generation. The square symbol marks the first and best cost of this generation and the remaining costs grow monotonically with their indices. The curve formed by the square symbols unveils the best performance from generation 1 to 7. The parameters associated with the best control law in each generation vary with increasing generation number $G$; so does the corresponding $K_e$ (figure 6*b*). The $f_e/f_0$ of the best performing individual converges to 0.52 at $G = 2$. The effective excitation at the subharmonic of $f_0$ has been previously reported by e.g. Freund & Moin (2000) and Wu *et al.* (2018*a*). With $G$ increasing from 1 to 6, $C_m$ and $\alpha$ gradually decline from 2.0 % and 50 % to 1.2 % and 7 %, respectively, the resulting $K_e$ grows from 0.40 to 0.51. Interestingly, the ratio $C_m/\alpha$ correlates well with $K_e$; in general, a larger $C_m/\alpha$ leads to a higher $K_e$. The converged $f_e/f_0$, $\alpha$ and $C_m$ are almost identical to those found from the conventional GP-based AI control (Wu *et al.* 2018*a*) where the optimal $C_m$ is predetermined from conventional open-loop control with $f_e/f_0$ and $\alpha$ fixed at 0.5 and 0.15, respectively. This comparison demonstrates that the present hybrid AI system is capable of optimizing simultaneously $C_m$ and the multi-frequency forcing law in the context of a more complex control landscape.

At other *Re* values, the learning curve is qualitatively the same as shown in figure 6(*a*). Nevertheless, the parameters associated with the best control law in each generation may exhibit different variations. The best control law of each generation is always associated

with a single $f_e/f_0$, approximately 0.52, at $Re < 10\,000$ but may be characterized by multiple frequencies, as seen from the power spectra (not shown) of the control signals, at $Re > 10\,000$, e.g. at $G = 3$ in figure 6(c), which presents the evolution of the control parameters associated with the best individual in each generation, and the corresponding $K_e$. Nevertheless, the multiple frequencies always reduce to a single frequency $f_e/f_0 \approx 0.5$ once the learning process is converged.

Figure 7 presents the dependence on $Re$ of the maximum $K_e$, i.e. $K_{e,max}$, along with the corresponding control parameters under the optimal control law. Interestingly, $K_{e,max}$ is found to be approximately constant, at between 0.51 and 0.53, for the $Re$ range examined, that is, the best control performance is essentially unchanged and so is the optimal $f_e/f_0$ or $(f_e/f_0)_{opt}$ ($\approx 0.5$). This result reconfirms Wu *et al.*'s (2018b) finding from an adaptive control technique over $Re = 5800$–13 300. However, the other control parameters exhibit a significant variation with $Re$. The optimum $C_m$ or $C_{m,opt}$, the optimum duty cycle $\alpha_{opt}$ and the optimum pulse width $\tau_{opt}$ ($= \alpha_{opt}/f_{e,opt}$) of minijet injection decrease from 1.5 %, 25 % and 5.0 ms to 1.2 %, 7 % and 1.0 ms, respectively, from $Re = 5800$ to 8000 ($Re < Re_{cr}$). The value of $C_{m,opt}$ rises gradually from 1.2 % to 2.2 % from $Re = 8000$ to 40 000, suggesting a larger minijet momentum to maintain the penetration depth or the best control performance at a higher $Re$, which complies with our instinct. The observed distinct behaviours of the control parameters between the $Re$ ranges of 5800–8000 and 10 000–40 000 may have a link to the occurrence of the jet transition from laminar to turbulence in the range of $Re = 8000$–10 000 (Mi *et al.* 2013). As expected, the variations in $\alpha_{opt}$ and $\tau_{opt}$ are similar to each other. Given a fixed $C_m$, a smaller $\alpha$ or pulse width $\tau$ of minijet injection should lead to a higher injection velocity or momentum per pulse, thus catering the need for a higher momentum at larger $Re$. For the presently used electromagnetic valve, the nominal smallest $\tau$ achievable is 0.8 ms. This may explain why $\tau_{opt} \approx 0.8$ ms at $Re \geq 16\,000$. When $\tau_{opt}$ reaches its minimum for $Re = 24\,000$, a further increase in $Re$ will lead to a larger $\alpha_{opt}$ as $f_0$ and hence $f_{e,opt}$ rises with $Re$. Nevertheless, the inability to reduce $\tau$ further is compensated by the increased $C_m$ so that $K_{e,max}$ does not fall appreciably. There is a considerable increase in $\tau_{opt}$, reaching approximately 3.1 ms, from $Re = 8000$ to 10 700, but there is accordingly an appreciable rise in $C_m$ that acts to maintain the penetration depth and hence $K_{e,max}$. The observation points to that the hybrid AI control may find an optimum combination of $f_e/f_0$, $\alpha$ and $C_m$ to achieve $K_{e,max}$ for given $Re$.

For the purpose of comparison, figure 7 also includes the optimal parameters $(f_e/f_0)_{opt}$ ($\approx 0.5$), $\alpha_{opt}$ ($= 12.5$ %) and $\tau_{opt}$ ($\approx 1.0$ ms) obtained at $Re = 13\,300$ from the same experimental rig using a conventional AI control, with $C_m$ fixed at 1.2 %, as developed by Wu *et al.* (2018a). Their $(f_e/f_0)_{opt}$ is the same but $\alpha_{opt}$ and $\tau_{opt}$ are smaller than the present results; however, their $K_{e,max}$ ($= 0.48$) is 10 % lower than the present result, apparently resulting from the fixed $C_m$ ($= 1.2$ %), which is inadequate to achieve the maximum penetration depth at $Re = 13\,300$.

The inter-relation between the control laws and associated evolution may be presented via a proximity map (Duriez, Brunton & Noack 2016). The idea is to represent control laws $\boldsymbol{b}(t)$ as points in a two-dimensional feature plane $\boldsymbol{\gamma}_j = (\gamma_{j,1}, \gamma_{j,2})$, where $j = 1, 2,\ldots,$ $N_i \times G$, so that the distance between feature vectors best manifests the difference between the control laws. How to define a distance matrix $D_{jk}$ ($j, k = 1, 2,\ldots, N_i \times G$) between the $j$th and $k$th $\boldsymbol{b}(t)$ is crucial in forming this feature plane. For the present actuation, this matrix is the averaged squared Euclidean difference between the actuation command vectors, given by

$$D_{jk}^2 = ||PSD(\boldsymbol{b}_{1,j}(t)) - PSD(\boldsymbol{b}_{1,k}(t))||^2 + \beta|b_{2,j} - b_{2,k}| + \delta|J_j - J_k|. \tag{4.1}$$

The first term on the right side of (4.1) is the square of the averaged Euclidean distance between $b_{1,j}(t)$ and $b_{1,k}(t)$ in the frequency domain, and thus the power spectral density functions (PSD) of $b_{1,j}(t)$ and $b_{1,k}(t)$ are used. The second term is the difference between $b_{2,j}$ and $b_{2,k}$ weighted by a factor $\beta$. The control performance $J$ weighted by a factor $\delta$ is also incorporated in (4.1). The parameters $\beta$ and $\delta$ may act to smooth the control landscape and are chosen so that the maximum differences in the three terms are the same, viz.

$$\max_{j,k=1,2\ldots N_i \times G} ||PSD(b_{1,j}(t)) - PSD(b_{1,k}(t))||^2 = \beta \max_{j,k=1,2\ldots N_i \times G} |b_{2,j} - b_{2,k}|$$
$$= \delta \max_{j,k=1,2\ldots N_i \times G} |J_j - J_k|. \tag{4.2}$$

Given $D_{jk}$, feature vectors $\boldsymbol{\gamma}_j$ ($j = 1, 2, \ldots, N_i \times G$) can be obtained by a classical multi-dimensional scaling (Cox & Cox 2000) so that the distances are optimally preserved

$$\sum_{j=1}^{N_i \times G} \sum_{k=1}^{N_i \times G} (||\boldsymbol{\gamma}_j - \boldsymbol{\gamma}_k|| - D_{jk})^2 = \min. \tag{4.3}$$

The feature vectors are sorted and rotated so that the first coordinate is characterized by the largest variance, the second by the second largest, etc. Finally, control laws can be visualized on a scatter plot or proximity map, as done by Kaiser *et al.* (2017) and Wu *et al.* (2018*a*). The map provides an overall picture of the control landscape, and the feature coordinates may correlate with some features of control, as shown by Zhou *et al.* (2020).

Figure 8(*a*) shows the proximity map of all control laws obtained in the learning process at $Re = 8000$ in a three-dimensional plane ($\gamma_1$, $\gamma_2$, $C_m/\alpha$). The addition of the third coordinate is due to the fact that $C_m/\alpha$ is well correlated with $K_e$ (figure 6*b*). Each circular symbol represents one control law and its colour corresponds to the value of $J$. Given $\gamma_1$ (or $\gamma_2$), we randomly select the control laws at different $\gamma_2$ (or $\gamma_1$) in figure 8(*a*) and examine carefully the control parameters, which unveils that $\gamma_1$ tends to be positively correlated with $C_m$ and $\gamma_2$ is adversely correlated with $\alpha$ for given $\gamma_1$. Furthermore, $C_m/\alpha$ is adversely correlated with $J$ or positively with $K_e$ (figure 8*a*), which is fully consistent with the fact that $C_m/\alpha$ corresponds physically to the penetration depth of the minijet into the main jet (Perumal & Zhou 2018). Similar observations are made at $Re = 20\,000$ (figure 8*b*).

## 5. Scaling Analysis

### 5.1. *Dependence of $K_0$ and $f_0$ on Re*

It is well known that the boundary-layer thickness at the jet exit diminishes with increasing $Re$, producing a significant influence on the flow structure development and accelerating the mixing rate (e.g. New *et al.* 2006; Mi *et al.* 2013) or centreline mean velocity decay rate of an unforced jet. Naturally, a manipulated jet is also sensitive to this change in the boundary-layer thickness. As such, $K_e = g_1$ ($C_m$, $f_e/f_0$, $\alpha$, $d/D$, $Re$, $K_0$), where $K_0$ is calculated by $K_0 = (\bar{U}_j - \bar{U}_{5D,0})/\bar{U}_j$. That is, the effect of boundary-layer thickness of the unforced jet on jet mixing is considered via $K_0$. Both $K_0$ and $f_0$ are dependent on $Re$.
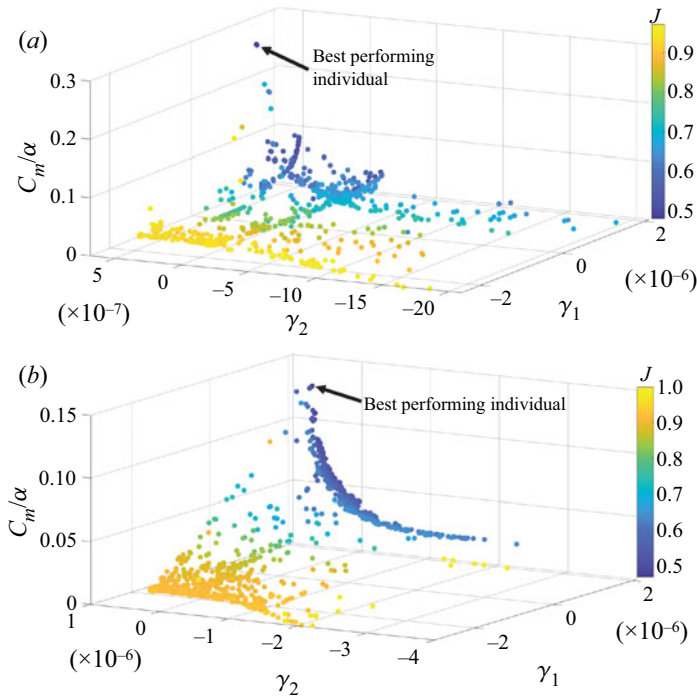
Figure 8. Control landscape based on a proximity map of all tested control laws at (*a*) $Re = 8000$ and (*b*) 20 000. Each circle represents an individual control law and the distance between two control laws indicates their dissimilarity.

As shown in figure 9,

$$K_0 = -103Re^{-0.83} + 0.1, \tag{5.1}$$

which rises rapidly with $Re$ for $Re \leq 10\,000$ but less so for $Re > 10\,000$. On the other hand, $f_0$ varies from 100 to 680 Hz (figure 9) and is linearly correlated with $Re$, viz.

$$f_0 = 0.0167Re + 16. \tag{5.2}$$

Both (5.1) and (5.2) are valid for $Re = 5800$–40 000.

### 5.2. *Dependence of $K_e/K_0$ on control parameters*

A careful analysis of experimental data from conventional open-loop control (Perumal & Zhou 2018) shows reasonably well collapsed $K_e/K_0$ for different $d/D$ provided that $C_m$ is re-scaled as $C_m(D/d)^{1-n}$. This collapse is illustrated for $Re = 13\,000$, where $1 - n = 0.55$ for $\alpha = 0.1$ (figure 10*a*1), 0.67 for $\alpha = 0.5$ (figure 10*b*1) and 1.00 for $\alpha = 0.9$ (figure 10*c*1). As a matter of fact, $n = -0.56\alpha + 0.50$, distinctly different from $n = -0.31\alpha + 0.28$ at $Re = 8000$ (Perumal & Zhou 2018) for the same $f_e/f_0$ ($= 0.5$). Interestingly, the same collapse is observed at $f_e/f_0 = 0.3$ and 1.0 (figure 10*a*2–*c*2) for $Re = 13\,000$ and $n$ is unchanged, although the magnitude of $K_e/K_0$ is different. The result suggests that $n$ is independent of $f_e/f_0$, that is, $n$ depends only on $\alpha$ for a given $Re$. Similar analysis has also been performed for other $Re$ values to determine the dependence of $n$ on $\alpha$ (figure 11*a*,*b*). In general,

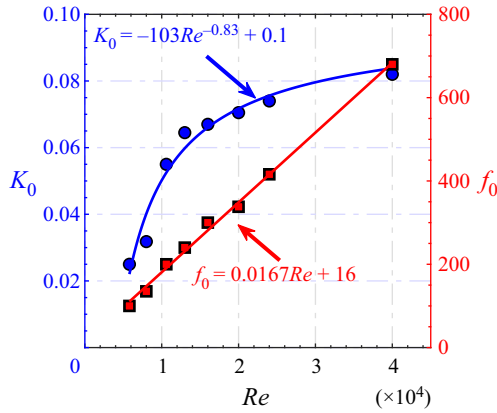$$n = C_1\alpha + C_2, \tag{5.3a}$$

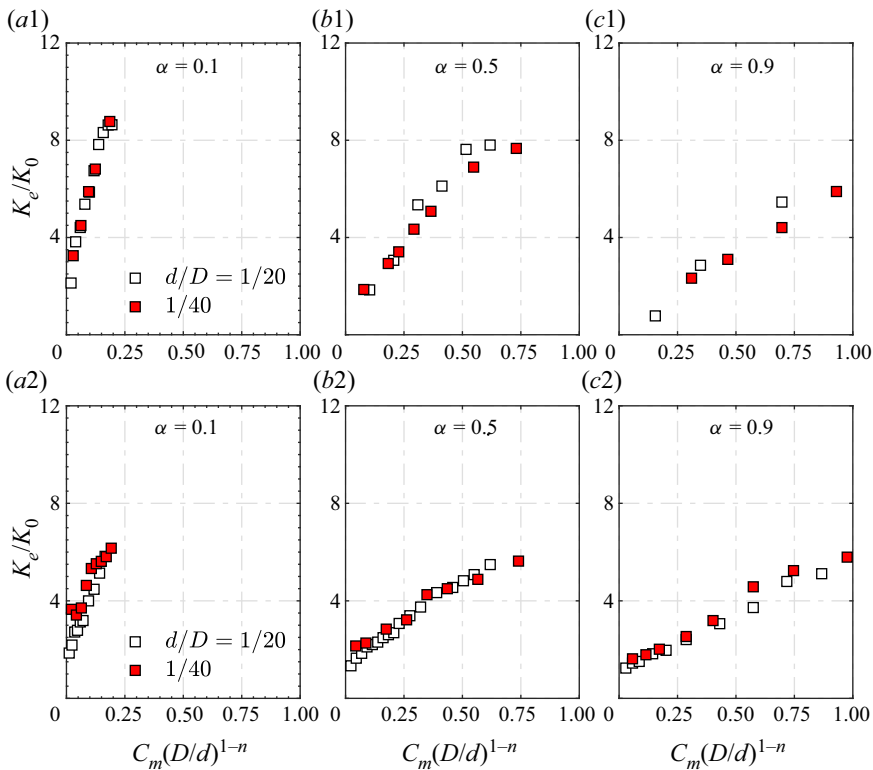Figure 9. Dependence of $K_0$ and $f_0$ on $Re$ for unforced jet.



Figure 10. Dependence of $K_e/K_0$ on $(C_m/\alpha)(D/d)^{1-n}$ for $Re = 13\,000$ at $(a1–c1)$ $f_e/f_0 = 0.5$ and $(a2–c2)$ 1.0.

where the coefficients $C_1$ and $C_2$ depend on $Re$, as shown in figure 11, given by

$$C_1 = \begin{cases} -9.64 \times 10^{-5} Re + 0.46, & 5800 \leq Re < 10\,600 \\ -0.56, & 10\,600 \leq Re \leq 40\,000 \end{cases}, \tag{5.3b}$$

$$C_2 = \begin{cases} 8.67 \times 10^{-5} Re - 0.42, & 5800 \leq Re < 10\,600 \\ 0.51, & 10\,600 \leq Re \leq 40\,000 \end{cases}. \tag{5.3c}$$
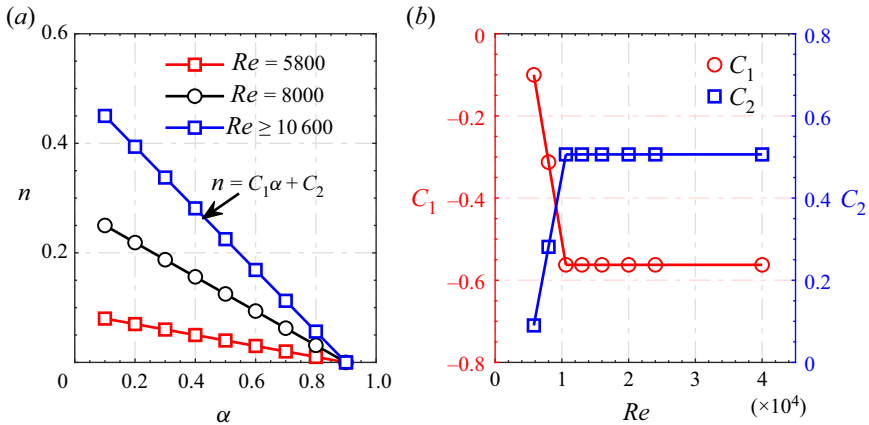
**942** A47-15

Figure 11. Dependence of (*a*) $n$ on $\alpha$; (*b*) $C_1$ and $C_2$ for $n = C_1 \alpha + C_2$ on $Re$.
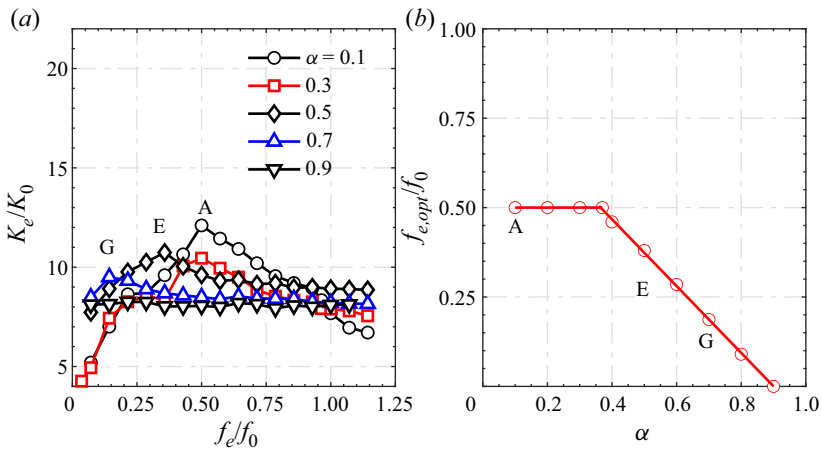


Figure 12. (*a*) Dependence of $K_e/K_0$ on $f_e/f_0$; (*b*) dependence of $f_{e,opt}/f_0$ on $\alpha$ ($Re = 8000$, $C_m = 1.0\,\%$, $d/D = 1/20$).

Apparently, $n$ depends only on $\alpha$ for $Re \geq 10\,600$ and is physically meaningful (to be discussed later).

The dependence of $K_e/K_0$ on $f_e/f_0$ is presented in figure 12(*a*) for $\alpha = 0.1$–0.7 ($Re = 8000$, $C_m = 1.0\,\%$, $d/D = 1/20$). We may extract the dependence on $\alpha$ of $f_{e,opt}/f_0$ at which the local maximum $K_e/K_0$ occurs, as shown in figure 12(*b*), viz.

$$\frac{f_{e,opt}}{f_0} = \begin{cases} 0.5, \alpha \leq 0.37 \\ -0.93\alpha + 0.84, \alpha > 0.37 \end{cases}. \tag{5.4}$$

It is worth mentioning that the $K_e/K_0$ data are not shown for $\alpha = 0.2$, 0.4 0.6 and 0.8 to avoid overcrowding in figure 12(*a*), although they are used to obtain figure 12(*b*). Similar analysis has been performed for other $Re$. Interestingly, $f_{e,opt}/f_0$ is independent of $Re$, as found by Wu *et al.* (2018*b*) for $Re = 5700$–13 300 (their figure 10*a*).

It would be difficult to develop a scaling law with $f_e/f_0$ incorporated since the dependence of $K_e/K_0$ on $f_e/f_0$ displays a distinct behaviour as $\alpha$ varies (figure 12*a*). Thus, we introduce $f_e/f_{e,opt} \equiv (f_e/f_0)/(f_{e,opt}/f_0)$, and $f_e/f_{e,opt} = 1$ corresponds to the local
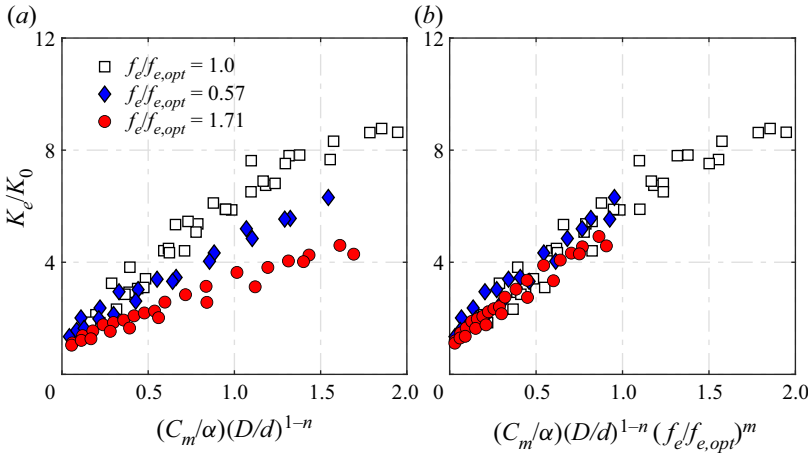
Figure 13. Dependence of $K_e/K_0$ on (*a*) $(C_m/\alpha)(D/d)^{1-n}$ for different $f_e/f_{e,opt}$ and (*b*) $(C_m/\alpha)(D/d)^{1-n}(f_e/f_{e,opt})^m$ ($\alpha = 0.1$–$0.9$; $Re = 13\,000$).

maximum $K_e/K_0$, irrespective of $\alpha$. Replotting the data in figure 10(*a*2–*b*2) in terms of the dependence of $K_e/K_0$ on $(C_m/\alpha)(D/d)^{1-n}$ for $f_e/f_{e,opt} = 1.00$, 0.57 and 1.71, we see a large departure from one $f_e/f_{e,opt}$ to another (figure 13*a*) but a reasonably good collapse if $(C_m/\alpha)(D/d)^{1-n}$ is replaced by $(C_m/\alpha)(D/d)^{1-n}(f_e/f_{e,opt})^m$ (figure 13*b*). The choice of power index $m$ is not so straightforward. As shown in figure 12(*a*), with increasing $f_e/f_0$, $K_e/K_0$ climbs for $f_e/f_0 \leq f_{e,opt}/f_0$ or $f_e/f_{e,opt} = (f_e/f_0)/(f_{e,opt}/f_0) \leq 1$ but declines for $f_e/f_0 > f_{e,opt}/f_0$ or $f_e/f_{e,opt} > 1$. One may surmise that the corresponding $m$ should be positive and negative, respectively. After numerous trial-and-error analyses, $m$ is found to be 0.7 and $-0.9$ for $f_e/f_0 \leq f_{e,opt}/f_0$ and $f_e/f_0 > f_{e,opt}/f_0$, respectively, which reflects the sensitivity of $K_e/K_0$ to the variation in $f_e/f_0$. It is further found that the $m$ values are unchanged as $Re$ varies from 5800 to 40 000, that is, $m$ is independent of $Re$. Nevertheless, the dependence of $K_e/K_0$ on $(C_m/\alpha)(D/d)^{1-n}(f_e/f_{e,opt})^m$ exhibits a large scatter as $Re$ varies from 5800 to 40 000 (figure 14). However, as shown in figure 15, it is, surprisingly, found that all the data of $K_e/K_0$, from more than 7000 AI-generated control laws or from conventional control (Perumal & Zhou 2018), collapse well together, with a small scatter, once a weighting factor $1/Re$ is introduced in the abscissa, i.e.

$$\zeta = \frac{C_m}{\alpha}\left(\frac{D}{d}\right)^{1-n}\frac{1}{Re}\left(\frac{f_e}{f_{e,opt}}\right)^m. \tag{5.5}$$

Here, $K_e = g_1\,(C_m, f_e/f_0, \alpha, d/D, Re, K_0)$ is now reduced to $K_e/K_0 = g_2\,(\zeta)$. The data may be least-square fitted to a cubic function, viz.

$$K_e/K_0 = 2.2 \times 10^{12}\zeta^3 - 1.3 \times 10^9\zeta^2 + 2.6 \times 10^5\zeta + 1.0. \tag{5.6}$$

The measured $K_e/K_0$ may deviate from (5.6) by no more than 10 %, with a 95 % confidence. Apparently, $K_e/K_0$ is the jet entrainment ratio, indicating the enhancement of entrainment with respect to the unforced jet.

One may wonder whether the same scaling law (5.6) could be obtained from a small amount of data, say generated by 200 control laws instead of 7000. One test is then performed. To ensure various control performances are covered, all the control laws for a given $Re$ are re-numbered based on their $J$ values, and 25 control laws are selected with
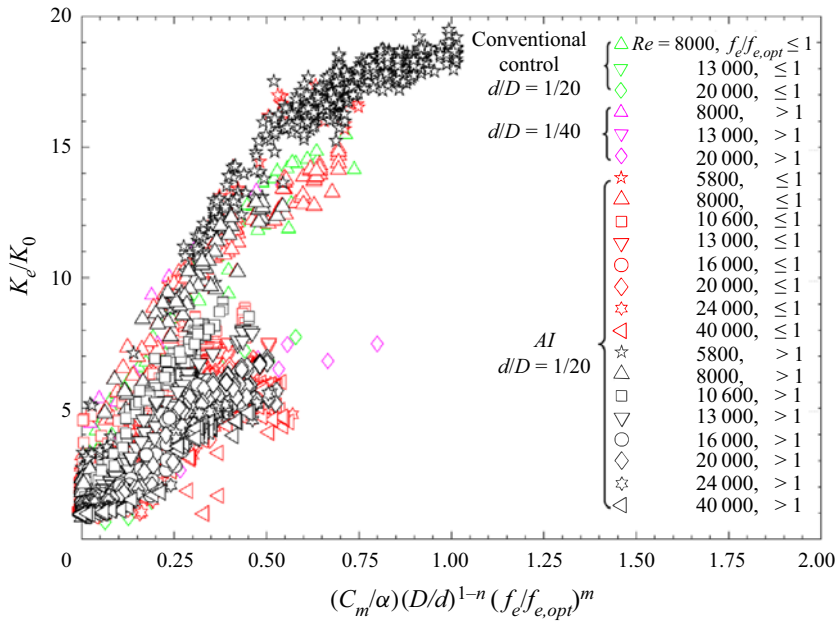
Figure 14. Dependence of $K_e/K_0$ on $(C_m/\alpha)(D/d)^{1-n}(f_e/f_{e,opt})^m$ for $Re = 5800$–$40\,000$ ($\alpha = 0.07$–$0.90$, $f_e/f_0 = 0.1$–$1.5$).
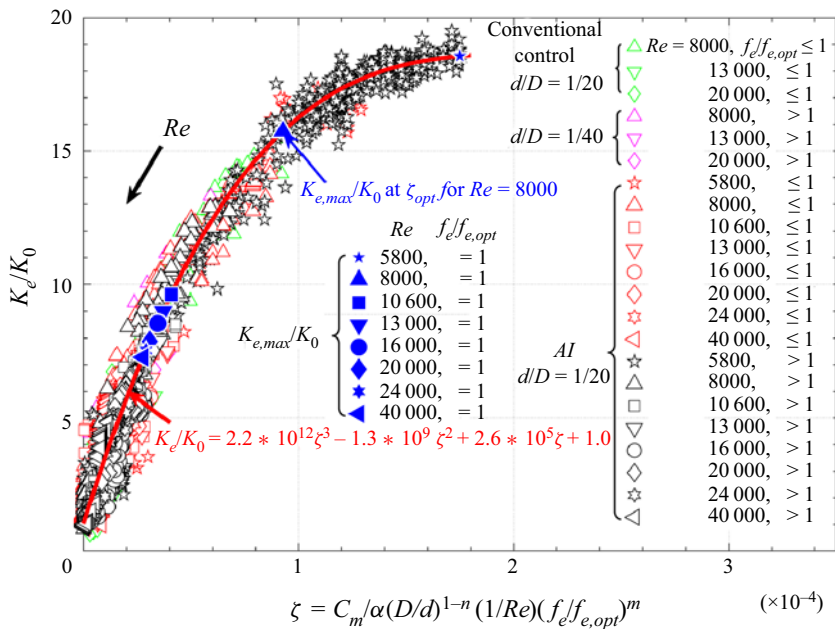


Figure 15. Dependence of $K_e/K_0$ on $(C_m/\alpha)(D/d)^{1-n}(1/Re)(f_e/f_{e,opt})^m$ for $Re = 5800$–$40\,000$, $\alpha = 0.07$–$0.9$, $f_e/f_0 = 0.1$–$1.5$. The red curve is the least-squares fit to experimental data. Blue filled symbols correspond to $K_{e,max}/K_0$, predicted from (5.6), at a given $Re$.
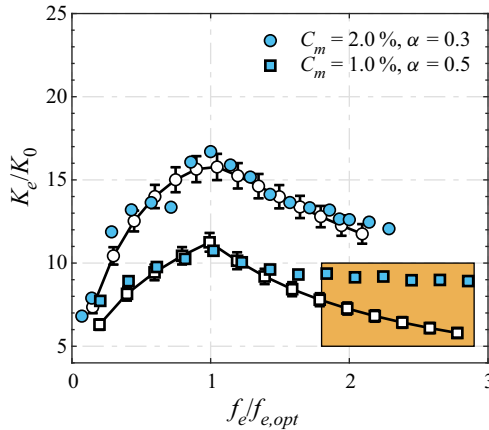
Figure 16. Comparison of the dependence of $K_e/K_0$ on $f_e/f_{e,opt}$ for $Re = 8000$ between prediction from (5.6) (open symbol) and measurement (filled symbol) for $(C_m, \alpha, d/D) = (2.0\%, 0.3, 1/20)$ and $(1.0\%, 0.5, 1/20)$. The rectangle highlights the deviation between prediction and measurement.

the same difference in $J$. The dependence of $K_e/K_0$ on $(C_m/\alpha)(D/d)^{1-n}(1/Re)(f_e/f_{e,opt})^m$ (figure not shown) can be least-squares fitted to a curve almost identical to that shown in figure 15, albeit with very few data falling between $\zeta = (1.0–1.9) \times 10^{-4}$, where $Re$ is 5800. One may conclude that the confidence level of the scaling law would not drop appreciably in spite of a drop in the control laws from the order of 1000 to 25 for each $Re$, given $Re \geq 8000$.

The way $m$ is determined may imply a limited range of $f_e/f_{e,opt}$ over which (5.6) is valid. As illustrated in figure 16, $K_e/K_0$ calculated from (5.6) agrees with measurement for $Re = 8000$ at $(C_m, \alpha, d/D) = (1.0\%, 0.5, 1/20)$ and $(2.0\%, 0.3, 1/20)$, thus providing a validity for the choice of $m$. Note an appreciable deviation for $f_e/f_{e,opt} \geq 1.8$ in $K_e/K_0$ between calculation and measurement at $\alpha = 0.5$. The measured $K_e/K_0$ appears to change little for $f_e/f_{e,opt} \geq 1.8$. Perumal & Zhou (2018) demonstrated that an unsteady minijet at large $\alpha$ ($\geq 0.5$) and $f_e/f_0$ ($\geq 1.0$) behaves like a quasi-steady blowing, and jet mixing is independent of both $\alpha$ and $f_e/f_0$, which accounts for the deviation. The observation suggests a critical $f_e/f_{e,opt}$ beyond which the scaling law (5.6) is invalid, and this critical $f_e/f_{e,opt}$ is the $f_{e,steady}/f_{e,opt}$ value at which $K_e/K_0$ becomes independent of $f_e/f_{e,opt}$ for a given $\alpha$. Figure 17 presents the dependence on $\alpha$ of $f_{e,steady}/f_0$, which is extracted from the data illustrated in figure 12(*a*) and least-square fitted to

$$f_{e,steady}/f_0 = -1.55\alpha^{1.1} + 1.4. \tag{5.7}$$

Then, the critical $f_e/f_{e,opt}$ or $f_{e,steady}/f_{e,opt}$ at which (5.6) may deviate appreciably from the measured data can be obtained from (5.4) and (5.7), viz.

$$\frac{f_{e,steady}}{f_{e,opt}} = \frac{f_{e,steady}/f_0}{f_{e,opt}/f_0}. \tag{5.8}$$

Substitution of $\alpha = 0.5$ into (5.4) and (5.7) yields $f_{e,steady}/f_{e,opt} = 1.8$, which is internally consistent with the observation from figure 16.

There is a need to understand the physical meaning of $n$, which may offer valuable insight into the flow physics behind control. The physical interpretation of $n$ is given by Perumal & Zhou (2018) for a fixed $Re$. As $d/D$ is decreased, say by half, one might have

expected, given $\alpha = 0.1$ and $f_e/f_0 = 0.5$, that the required $C_m$ would also reduce by 50 % to achieve the same $K_e/K_0$ ($Re = 8000$); yet, $C_m$ was measured to drop by 60 % (their figure 23). The additional 10 % drop results from the retardation effect of minijet injection with contracting $d/D$. That is, a non-zero $n$ reflects the need for additional $C_m$ to achieve the same $K_e/K_0$ for given $\alpha$. Apparently, the retardation effect depends on $\alpha$ and $Re$ (5.3). Perumal & Zhou (2018) have documented in detail the dependence of the retardation effect on $\alpha$. Thus, we present only its dependence on $Re$. In order to determine the dependence of required $C_m$ on $Re$ to achieve the same $K_e/K_0$ at given $f_e/f_{e,opt}$, $\alpha$ and $d/D$, we rewrite (5.6) as

$$K_e/K_0 \approx \frac{C_m}{\alpha}\left(\frac{D}{d}\right)^{1-n}\frac{1}{Re}\left(\frac{f_e}{f_{e,opt}}\right)^m. \tag{5.9}$$

Rearranging (5.9) yields

$$C_m \approx Re K_e/K_0\alpha\left(\frac{d}{D}\right)^{1-n}\left(\frac{f_{e,opt}}{f_e}\right)^m. \tag{5.10}$$

Equation (5.10) can be used to predict the required $C_m$ with varying $Re$ for a pre-specified $K_e/K_0$ at given $f_e/f_{e,opt}$, $\alpha$ and $d/D$. It is of interest to compare the variation in $C_m$ with $Re$ for a given $K_e/K_0$ at the same $f_e/f_{e,opt}$, $\alpha$ and $d/D$ with and without the retardation effect. On substitution of $n = 0$ in (5.10), we may obtain $C_m$ in the absence of the retardation effect

$$C_m \approx Re K_e/K_0\alpha\left(\frac{d}{D}\right)\left(\frac{f_{e,opt}}{f_e}\right)^m. \tag{5.11}$$

Figure 18 compares the dependence of $C_m$ on $Re$ ($= 5800$–$40\,000$) for a pre-specified $K_e/K_0 = 6$ ($f_e/f_{e,opt} = 1.0$, $\alpha = 0.1$, $d/D = 1/20$) calculated from (5.11) with that from (5.10) where $n$ is determined from (5.3a–c). Clearly, given the same $Re$, $C_m$ calculated from (5.10) is substantially larger, as a result of the retardation effect, than that from (5.11). For example, at $Re = 20\,000$, the $C_m$ values from (5.10) and (5.11) are approximately 0.85 % and 0.22 %, respectively. The retardation effect may depend on $Re$, which is defined by the percentage increase in required $C_m$ calculated from (5.10) as compared with (5.11), viz.

$$\Delta C_m = ([C_m]_{(5.10)} - [C_m]_{(5.11)})/[C_m]_{(5.11)}. \tag{5.12}$$

The value of $\Delta C_m$ increases with $Re$ for $Re < 10\,600$ and becomes independent of $Re$ for $Re \geq 10\,600$ (figure 18), as $n$ does (figure 11b). At $Re = 20\,000$, the required $C_m$ to achieve a pre-specified $K_e/K_0 = 6$ ($f_e/f_{e,opt} = 1.0$, $\alpha = 0.1$, $d/D = 1/20$) from (5.10) is 2.8 times higher than from (5.11). Evidently, $n$ plays a significant role in characterizing the retardation effect of the minijet, which contracts with increasing $\alpha$ and reaches zero at $\alpha = 0.9$, where $n \approx 0$ (Perumal & Zhou 2018).

### 5.3. *Physical interpretation of similarity parameters*

Some interesting inferences can be made from the scaling law (figure 15 or (5.6)). Firstly, it is important to understand physically $\xi/Re$, where $\xi = (C_m/\alpha)(D/d)^{1-n}$ is interpreted as the effective penetration depth at a given $Re = 8000$ (Perumal & Zhou 2018). Yang *et al.* (2016) and Perumal & Zhou (2018) demonstrated that the distribution of $u_{rms}^*$ at the nozzle exit and the minijet penetration depth into the main jet are correlated. Figure 19 shows the radial distributions of $u_{rms}^* = u_{rms}/\bar{U}_j$ measured at $x^* = 0.05$ ($f_e/f_{e,opt} = 1$) along the injection ($x$–$y$) plane for $\xi/Re = 0.3 \times 10^{-4}$ at $Re = 8000$, 13 000 and 20 000.
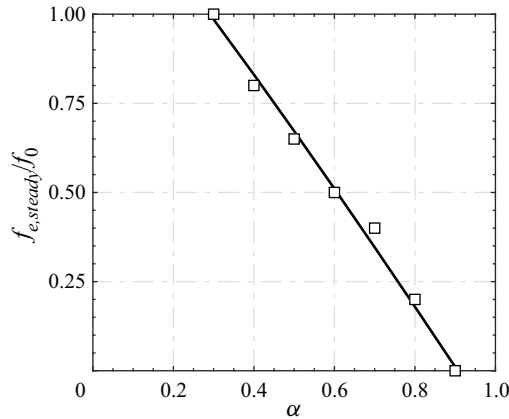
Figure 17. Dependence of $f_{e,steady}/f_0$ on $\alpha$ extracted from the dependence of $K_e/K_0$ on $f_e/f_0$, as illustrated in figure 12($a$).
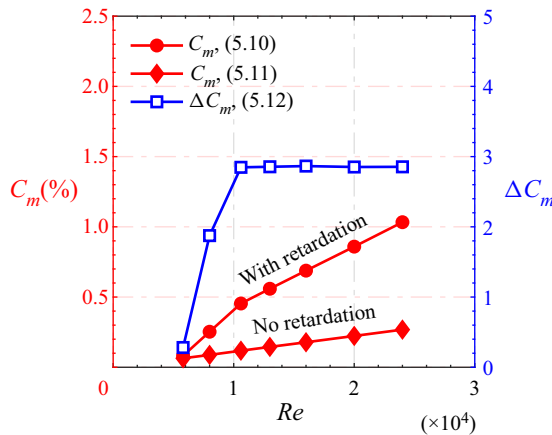


Figure 18. Dependence of $C_m$ and $\Delta C_m$ on $Re$ ($f_e/f_{e,opt} = 1.0$, $\alpha = 0.1$, $d/D = 1/20$) calculated from ((5.10)–(5.12)) for a pre-specified $K_e/K_0 = 6$.

Interestingly, given the same $\xi/Re$, the $u^*_{rms}$ distributions are qualitatively the same despite different combinations of $C_m$, $\alpha$, $d/D$ and $Re$, suggesting that the penetration depth, as marked in figure 19, is the same given the same $\xi/Re$, that is, there is a correspondence between $\xi/Re$ and the penetration depth. Perumal & Zhou (2018) pointed out that $\xi$ is physically the effective momentum ratio of the minijet to the main jet per pulse of injection or the effective penetration depth for a fixed $Re$. The present finding points to the fact that $\xi/Re$ is a more general definition for the effective momentum ratio of the minijet to the main jet per pulse of injection, which is valid even in the context of varying $Re$.

Secondly, to gain insight into the physics behind $f_e/f_{e,opt}$, we present in figure 20($a1$–$c2$) typical images from flow visualization ($Re = 8000$) in the injection plane ($x$–$z$) for $f_e/f_{e,opt} < 1$, $f_e/f_{e,opt} = 1$ and $f_e/f_{e,opt} > 1$ at $\xi/Re = 0.3 \times 10^{-4}$, along with the signals of instantaneous streamwise $U^*$ measured at $(x^*, y^*, z^*) = (1.5, 0, 0.45)$. The sharp peaks in the signals represent the perturbation induced by the injection. Once manipulated, the shear layer rolls up early on the injection side (cf. unforced flow shown in figure 3$b$) and the vortex dynamics is very different, depending on $f_e/f_{e,opt}$. There exist three different
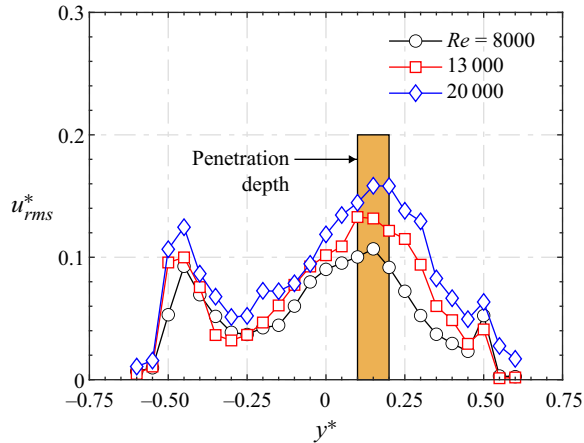
Figure 19. Radial distributions of the streamwise fluctuating velocity $u^*_{rms} = u_{rms}/\bar{U}_j$ measured at $x^* = 0.05$ ($f_e/f_{e,opt} = 1$) for $\xi/Re = 0.3*10^{-4}$.

states of the manipulated jet depending on $f_e/f_{e,opt}$. State 1 corresponds to $f_e/f_{e,opt} = 1$, at which the optimal separation takes place between incomplete ring vortices. As shown in figure 20($b$1), an incomplete ring vortex $V_2$ induced by minijet injection is advected downstream without direct interaction with a following vortex $V_1$ induced by the next cycle of injection. This assertion is complemented by the velocity signal in figure 20($a$1), where the peaks are distinctly separated. It seems plausible that the ring vortices with the minimum but clear separation produce the maximized jet decay rate (figure 16). State 2 corresponds to a smaller $f_e/f_{e,opt}$ ($= 0.57$) or an increased gap between the successive ring vortices, as shown in figure 20($a$2,$b$2). Evidently, the incomplete ring vortex $V_4$ needs more time to grow before interacting with the next one $V_3$. This increased gap seems to facilitate the establishment of less anti-symmetrically arranged vortices about the centreline in the ($x$–$y$) plane (figure 20$a$2, cf. figure 20$a$1), resembling more a natural jet and resulting in a reduced jet decay rate (figure 16). Under state 3, where $f_e/f_{e,opt} > 1$, the spatial separation between the vortices $V_5$ and $V_6$ contracts, as illustrated in figure 20$c$2 ($f_e/f_{e,opt} = 1.71$), and the interaction between the vortices is intensified. This is corroborated by the hot-wire signal (figure 20$c$1), which shows the peaks closely separated from each other. This interaction may incur the occurrence of turbulent puff-like structures, causing a retreat of penetration (Hermanson, Wahba & Johari 1998; Johari 2006) and weakened mixing. Johari, Pacheco-Tougas & Hermanson (1999) made a similar observation for jet in cross-flow and pointed out that a decrease in spacing between the vortical structures resulted in increased interaction and reduced penetration. Thus, the jet decay rate under state 3 also drops compared with state 1 (figure 16). The three states observed at $Re = 8000$ are also evident at other $Re$ (not shown) given an identical $\xi/Re$. The similarity parameter $f_e/f_{e,opt}$ on which states 1–3 strongly depend physically corresponds to the spatial separation between successive vortices formed during minijet injection (figure 20$a$2–$c$2). Thus, the jet mixing depends on the penetration depth of the minijet into the main jet ($\xi/Re$) and the interaction between vortices ($f_e/f_{e,opt}$) in the manipulated jet, and $\zeta$ is physically the momentum ratio (the momentum per pulse of injection to the inertia momentum of main jet) times the frequency ratio.
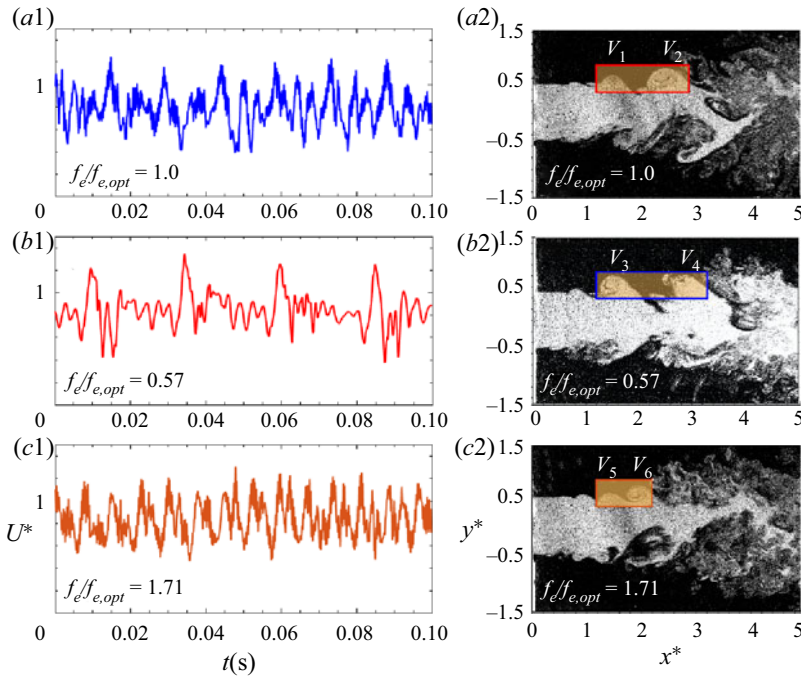
**942** A47-22

Figure 20. ($a1$–$c1$) Typical $U^*$ signals measured at $(x^*, y^*, z^*) = (1.5, 0, 0.45)$ for $f_e/f_{e,opt} = 0.57$, 1 and 1.71 at $\xi/Re = 0.3 \times 10^{-4}$ for $Re = 8000$. ($a2$–$c2$) Typical flow structures from flow visualization in the injection plane ($x$–$z$) at representative $f_e/f_{e,opt}$, where the vortices $V_1$–$V_6$ result from minijet injection at $\xi/Re = 0.3 \times 10^{-4}$ for $Re = 8000$.

Thirdly, the ratio $K_{e,max}/K_0$ drops rapidly with increasing $Re$ for $Re < 10\,600$ but very slowly for $Re \geq 10\,600$ (figure 21), which may be described by

$$K_{e,max}/K_0 \approx 2.24 * 10^{15} Re^{-3.7} + 6.8. \tag{5.13}$$

This feature is primarily due to the variation in $K_0$ with increasing $Re$ (figure 9) as $K_{e,max}$ is unchanged (figure 7). As such, $\zeta = (\xi/Re)(f_e/f_{e,opt})^m$ and $\xi_{opt} = ((\sqrt{MR}/\alpha)(d/D)^n)_{opt}$ at which $K_{e,max}/K_0$ occurs. Then, at $f_e/f_{e,opt} = 1$, (5.9) may be rewritten as

$$K_{e,max}/K_0 \approx \left( \frac{\sqrt{MR}}{\alpha} \left( \frac{d}{D} \right)^n \right)_{opt} \frac{1}{Re} \left( \frac{f_{e,opt}}{f_{e,opt}} \right)^{0.7} = \frac{\xi_{opt}}{Re} = \zeta_{opt}. \tag{5.14}$$

Thus, given $Re$, $K_{e,max}/K_0$ may be estimated from (5.13). As $\zeta_{opt} = \xi_{opt}/Re$ is connected to the effective penetration depth of the minijet into main jet and hence $K_e/K_0$, the drop in $K_{e,max}/K_0$ with $Re$ can be directly correlated to the reduced effective minijet penetration into main jet measured in terms of $\xi_{opt}/Re$. One may wonder why the effective penetration depth or $\xi_{opt}/Re$ contracts with increasing $Re$. Figure 21 presents a variation with $Re$ in the normalized stroke length $L/d$ determined at $K_{e,max}/K_0$. Physically, $L$ represents the slug of jet fluid ejected during each pulse of injection or the amount of fluid injected during one injection (Steinfurth & Weiss 2020) and, following Johari (2006), is estimated by $L = (1/A_m) \int_0^{\tau_{opt}} \int_A U_m \, dA_m \, dt = \bar{U}_m \tau_{opt}$, where $\tau_{opt} = \alpha/f_{e,opt}$, the minijet velocity $\bar{U}_m = C_m (D/d)^2 \bar{U}_j$ (Perumal & Zhou 2018) and $A_m$ is the minijet exit area. Johari (2006) found that the minijet-generated flow structure depended on $L/d$, characterized by
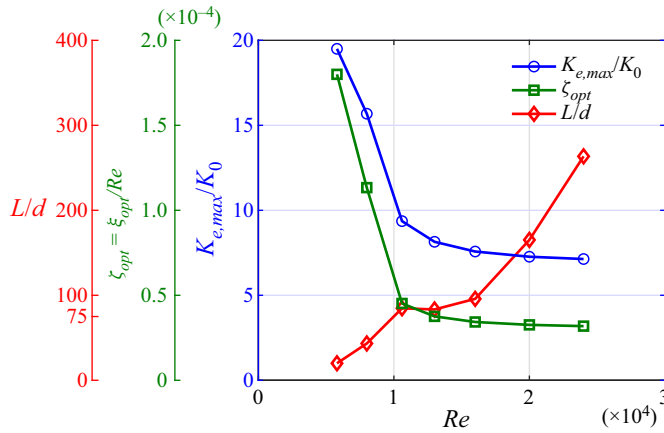
Figure 21. Dependence of $K_{e,max}/K_0$ on $Re$ extracted from figure 7, and $\zeta_{opt}(= \xi_{opt}/Re)$ on $Re$ at $K_{e,max}/K_0$ ($f_e/f_{e,opt} = 1.0$) obtained from (5.14) and the variation of stroke length ratio $L/d$ with increasing $Re$ when the control performance is optimal ($f_e/f_{e,opt} = 1.0$).
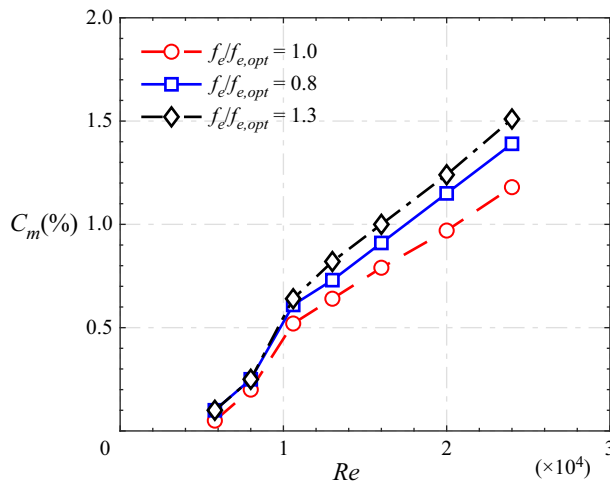


Figure 22. Dependence of $C_m$ on $Re$ for $f_e/f_{e,opt} = 1.0$, $< 1.0$ and $> 1.0$ ($\alpha = 0.1$, $d/D = 1/20$), predicted from (5.10) for a pre-defined $K_e/K_0 = 6$.

turbulent puffs for $25 < L/d < 75$ and an elongated steady jet structure for $L/d > 75$, and the penetration depth of the latter was significantly smaller than that of the former. Figure 21 shows that $L/d$ grows with $Re$ and indeed exceeds 75 for $Re \geq 10\,600$. This provides an explanation for the observation that $K_{e,max}/K_0$ or $\xi_{opt}/Re$ drops greatly from $Re = 8000$ to $10\,600$ (figure 21).

Fourthly, given a pre-specified $K_e/K_0 = 6$ and $(\alpha, d/D) = (0.1, 1/20)$, we may determine the relation between $C_m$ and $Re$ from (5.10) for $f_e/f_{e,opt} = 0.57$, 1.0 and 1.71. Figure 22 shows that $C_m$ is always least at $f_e/f_{e,opt} = 1.0$, regardless of $Re$.

Finally, Wickersham (2007) investigated the effect of excitation frequency of pulsed injection on a jet of $Re = 71\,000$–$355\,000$ manipulated by two pulsed injections. They argued that, under the optimal pulsing condition, the minijet penetrated farther into the jet and the induced vortices were able to persist longer downstream, thus enhancing mixing.

**942** A47-24

In the study of a pulsed jet in cross-flow, Johari (2006) also reported that the maximum mixing can be achieved with pulsed jets if the pulsing parameters are chosen specifically to create compact vortex rings and subsequent interaction among vortical structures. Nevertheless, to the best of our knowledge, there has been no report in the literature on the parameters that determine the optimal pulsing condition. This condition is evident from (5.14), determined by $\xi_{opt}/Re$ and $f_e/f_{e,opt} = 1$, and hence $\zeta_{opt}$, that is, $K_{e,max}/K_0$ is achieved at the maximum penetration $\xi_{opt}/Re$ and meanwhile the vortices thus formed under minijet injection are optimally separated from each other, as dictated by $f_e/f_{e,opt} = 1$.

## 6. Conclusions

A novel hybrid AI system has been developed to manipulate a turbulent jet using a single pulsed radial minijet over a range of $Re$ ($= 5800$–$40\,000$). Four control parameters are investigated, i.e. $C_m$ ($= 0.1\,\%$–$8.0\,\%$), $f_e/f_0$ ($= 0$–$1.2$), $\alpha$ ($= 0.1$–$0.9$) and $d/D$ ($= 1/20$, $1/40$). The following conclusions can be drawn out of this work:

(i) The developed hybrid AI algorithm may optimize simultaneously a control law and a time-independent variable $C_m$, overcoming the drawback of the previous AI system based on the LGP algorithm that can be used to optimize only the control laws (e.g. Zhou *et al.* 2020). At $Re = 8000$, for example, the system successfully finds the optimal control law, which consists of two sub-control laws that govern a time-dependent pulse signal $\boldsymbol{b}_1(t)$ ($\alpha = 7\,\%$, $f_e/f_0 = 0.52$) and a time-independent mass flow rate signal $b_2$ ($C_m = 1.2\,\%$), respectively. Proximity map analysis performed based on all the control laws reveals that the ratio $C_m/\alpha$, corresponding physically to the penetration depth of the pulsed minijet, dictates the control performance (figure 8). The system exhibits good robustness as $Re$ varies from 5800 to 40 000, finding essentially the same maximum $K_e$ and the same optimal $f_e/f_0$.

(ii) The AI system produces more than 7000 control laws for eight $Re$ values examined and subsequently a tremendous amount of data involving six intrinsically related variables $K_e$, $K_0$, $C_m$, $f_e/f_0$, $\alpha$ and $Re$. Careful analysis of the data, along with those produced from a conventional open-loop control technique, which include one more variable, $d/D$, unveils, surprisingly, a scaling law, that is, the relationship $K_e = g_1 (C_m, f_e/f_0, \alpha, d/D, Re, K_0)$ may be reduced to $K_e/K_0 = g_2 (\zeta)$, where the scaling factor $\zeta = (C_m/\alpha)(D/d)^{1-n}(1/Re)(f_e/f_{e,opt})^m$. This law governs the effect of $Re$ on jet manipulation using an unsteady minijet. Here, $K_e/K_0$ accounts for the effect of $Re$ on the control performance, while $\zeta$ is physically the momentum ratio $(C_m/\alpha)(D/d)^{1-n}(1/Re)$ (the momentum per pulse of minijet injection to the inertia momentum of the main jet) times the frequency ratio $(f_e/f_{e,opt})^m$, the latter providing a measure for the spatial separation between successive vortices (figure 20$a$2–$c$2). The manipulated jet may exhibit three states, i.e. state $1 - f_e/f_{e,opt} = 1$, state $2 - f_e/f_{e,opt} > 1$ and state $3 - f_e/f_{e,opt} < 1$, dictated by $(f_e/f_{e,opt})^m$. State 1 is associated with the optimally separated vortices, resulting in $K_{e,max}/K_0$, while states 2 and 3 yield closely and over-separated vortices, respectively, both causing a decline in $K_e/K_0$ (figure 16).

(iii) Several inferences can be made from the scaling law. Firstly, $K_e/K_0$ increases with $\zeta$. Secondly, given that $\xi = (C_m/\alpha)(D/d)^{1-n}$ may be interpreted as the effective momentum ratio of the minijet per pulse of injection to the main jet at a given $Re$ (Perumal & Zhou 2018), $\xi/Re$ carries the same physical meaning, although with a more general sense, valid even in the context of varying $Re$. Thirdly, with

$\zeta = (\xi/Re)(f_e/f_{e,opt})^m$, $\zeta_{opt}$ at which $K_{e,max}/K_0$ occurs for any given $Re$ depends on $\xi_{opt}$ and $(f_e/f_0)^m_{opt}$. The value of $\xi_{opt}$ drops from $Re = 8000$ to 10 600 and then rises for a further increase in $Re$ (figure 21). Evidently, jet mixing depends on both the penetration depth and the interaction between vortices or $\xi/Re$ and $(f_e/f_{e,opt})^m$, whose optimum values lead to the maximized mixing. The optimal pulsing condition at which the maximum effective penetration of the minijet into the main jet occurs corresponds to $\xi_{opt}$ (Wickersham 2007). At $f_e/f_{e,opt} = 1$, the minijet creates compact vortex rings (Johari 2006), which may persist farther downstream (Wickersham 2007), thus maximizing jet mixing. The similarity parameter $\zeta$ unveils that, for given $\alpha$, the required $C_m$ to achieve a pre-defined jet mixing or a constant $K_e/K_0$ is the smallest at $f_e/f_{e,opt} = 1$ or the most efficient, irrespective of $Re$ (figure 22). Finally, with increasing $Re$, $K_{e,max}/K_0$ diminishes rapidly for $Re < 10\ 600$ but very slowly for $Re \geq 10\ 600$ (figure 21). The stroke length ratio $L/d$ rises with $Re$ (figure 21). Once $L/d$ exceeds 75, the minijet flow structure is characterized by turbulent puffs, associated with the distributed vorticity and greater entrainment rate (Johari 2006), instead of vortex rings, resulting in a reduced effective penetration depth and hence a smaller $K_{e,max}/K_0$.

**Declaration of interests.** The authors report no conflict of interest.

**Author ORCIDs.**

- A.K. Perumal https://orcid.org/0000-0002-0547-5609;

- Z. Wu https://orcid.org/0000-0001-8495-1740;

- D.W. Fan https://orcid.org/0000-0002-2652-4414.

## REFERENCES

ARBEY, H. & WILLIAMS, J.F. 1984 Active cancellation of pure tones in an excited jet. *J. Fluid Mech.* **149**, 445–454.

BEAUDOIN, J.F., CADOT, O., AIDER, J.L. & WESFREID, J.E. 2006 Drag reduction of a bluff body using adaptive control methods. *Phys. Fluids* **18** (8), 085107.

BREIDENTHAL, R.E., TONG, K.-O., WONG, G.S., HAMERQUIST, R.D. & LANDRY, P.B. 1985 Turbulent mixing in two-dimensional ducts with transverse jets. *AIAA J.* **21** (11), 1867–1869.

BRUNTON, S.L. & NOACK, B.R. 2015 Closed-loop turbulence control: progress and challenges. *Appl. Mech. Rev.* **67** (5), 050801:01-48.

CHOI, H., MOIN, P. & KIM, J. 1994 Active turbulence control for drag reduction in wall-bounded flows. *J. Fluid Mech.* **262**, 75–110.

COX, T. & COX, M. 2000 *Multidimensional Scaling*. Chapman & Hall.

CROW, S.C. & CHAMPAGNE, F.H. 1971 Orderly structure in jet turbulence. *J. Fluid Mech.* **48**, 547–591.

DURIEZ, T., BRUNTON, S.L. & NOACK, B.R. 2016 *Machine Learning Control — Taming Nonlinear Dynamics and Turbulence, Fluid Mechanics and Its Applications*, vol. 116. Springer-Verlag.

FAN, D.W., WU, Z., YANG, H., LI, J.D. & ZHOU, Y. 2017 Modified extremum-seeking closed-loop system for jet mixing enhancement. *AIAA J.* **55** (11), 3891–3902.

FAN, D.W., ZHOU, Y. & NOACK, B.R. 2020 Fast triple-parameter extremum seeking exemplified for jet control. *Exp. Fluids* **61** (7), 152.

FREUND, J.B. & MOIN, P. 2000 Jet mixing enhancement by high-amplitude fluidic actuation. *AIAA J.* **38**, 1863–1870.

GAUTIER, N. & AIDER, J.L. 2013 Control of the separated flow downstream of a backward-facing step using visual feedback. *Proc. R. Soc.* A-*Math. Phys. Engng Sci.* **469** (2160), 20130404.

GAUTIER, N., AIDER, J.L., DURIZE, T., NOACK, B.R., SEGOND, M. & ABEL, M. 2015 Closed-loop separation control using machine learning. *J. Fluid Mech.* **770**, 442–457.

HENDERSON, B. 2010 Fifty years of fluidic injection for jet noise reduction. *Intl J. Aeroacoust.* **9**, 91–122.

HERMANSON, J.C., WAHBA, A. & JOHARI, H. 1998 Duty-cycle effects on penetration of fully modulated, turbulent jets in crossflow. *AIAA J.* **36**, 1935–1937.

HUSSEIN, H., CAPP, S. & GEORGE, W. 1994 Velocity measurements in a high-Reynolds-number, momentum-conserving, axisymmetric turbulent jet. *J. Fluid Mech.* **258**, 31–75.

JOHARI, H. 2006 Scaling of fully pulsed jets in crossflow. *AIAA J.* **44**, 2719–2725.

JOHARI, H., PACHECO-TOUGAS, M. & HERMANSON, J.C. 1999 Penetration and mixing of fully modulated turbulent jets in crossflow. *AIAA J.* **37** (7), 842–850.

KAISER, E., NOACK, B.R., SPOHN, A., CATTAFESTA, L.N. & MORZYŃSKI, M. 2017 Cluster-based control of a separating flow over a smoothly contoured ramp. *Theor. Comput. Fluid Dyn.* **31** (5), 579–593.

KIM, J. & BEWLEY, T. 2007 A linear systems approach to flow control. *Annu. Rev. Fluid Mech.* **39**, 383–417.

KNOWLES, K. & SADDINGTON, A.J. 2006 A review of jet mixing enhancement for aircraft propulsion applications. *Proc. IMechE Vol. 220 Part G: J. Aerosp. Engng* **220** (2), 103–127.

KOZA, J. R. 1990 Genetically breeding populations of computer programs to solve problems in artificial intelligence. In *[1990] Proceedings of the 2nd International IEEE Conference on Tools for Artificial Intelligence*, pp. 819-827. IEEE.

LI, R., NOACK, B.R., CORDIER, L., BOREE, J. & HARAMBAT, F. 2017 Drag reduction of a car model by linear genetic programming control. *Exp. Fluids* **58** (103), 1–20.

MI, J. & NATHAN, G.J. 2010 Statistical properties of turbulent free jets issuing from nine differently-shaped nozzles. *Flow Turbul. Combust.* **84** (4), 583–606.

MI, J., XU, M. & ZHOU, T. 2013 Reynolds number influence on statistical behaviors of turbulence in a circular free jet. *Phys. Fluids* **25**, 075101.

NEW, T.H., LIM, T.T. & LUO, S.C. 2006 Effects of jet velocity profiles on a round jet in cross-flow. *Exp. Fluids* **40** (6), 859–875.

NOACK, B.R. 2018 Closed-loop turbulence control—from human to machine learning (and retour). In *Proceedings of the 4th Symposium on Fluid Structure-Sound Interactions and Control (FSSIC), Tokyo, Japan* (ed. Y. Zhou, M. Kimura, G. Peng, A.D. Lucey & L. Hung), pp. 1–10. Springer.

NOACK, B.R, MORZYNSKI, M. & TADMOR, G. (Eds.) 2011 *Reduced-Order Modelling for Flow Control*, vol. 528. Springer Science & Business Media.

PANCHAPAKESAN, N.R. & LUMLEY, L.J. 1993 Turbulence measurements in axisymmetric jets of air and helium. Part 1. Air jet. *J. Fluid Mech.* **246**, 197.

PAREKH, D., LEONARD, A. & REYNOLDS, W.C. 1988 Bifurcating jets at high Reynolds numbers. *Department of Mechanical Engineering Thermosci. Div. Rep.* TF35. Stanford University.

PAREZANOVIĆ, V., *et al.* 2015 Mixing layer manipulation experiment. *Flow Turbul. Combust.* **94** (1), 155–173.

PASTOOR, M., HENNING, L., NOACK, B.R., KING, R. & TADMOR, G. 2008 Feedback shear layer control for bluff body drag reduction. *J. Fluid Mech.* **608**, 161–196.

PERUMAL, A.K. & RATHAKRISHNAN, E. 2022 Design of fluidic injector for supersonic jet manipulation. *AIAA J.* 1–10.

PERUMAL, A.K. & ZHOU, Y. 2018 Parametric study and scaling of jet manipulation using an unsteady minijet. *J. Fluid Mech.* **848**, 592–630.

PERUMAL, A.K. & ZHOU, Y. 2021 Axisymmetric jet manipulation using multiple unsteady minijets. *Phys. Fluids* **33** (6), 065124.

QIAO, Z.X., MINELLI, G., NOACK, B.R., KRAJNOVIĆ, S. & CHERNORAY, V. 2021 Multi-frequency aerodynamic control of a yawed bluff body optimized with a genetic algorithm. *J. Wind Engng Ind. Aerodyn.* **212**, 104600.

REYNOLDS, W.C., PAREKH, D.E., JUVET, P.J.D. & LEE, M.J.D. 2003 Bifurcating and blooming jets. *Annu. Rev. Fluid Mech.* **35** (1), 295–315.

RICOU, F.P. & SPALDING, D.B. 1961 Measurements of entrainment by axisymmetrical turbulent jets. *J. Fluid Mech.* **11**, 21.

SAMIMY, M., KIM, J.H., KASTNER, J., ADAMOVICH, I. & UTKIN, Y. 2007 Active control of high-speed and high-Reynolds-number jets using plasma actuators. *J. Fluid Mech.* **578**, 305–330.

STEINFURTH, B. & WEISS, J. 2020 Efficient vortex ring generation with non-parallel planar starting jets in crossflow. In *AIAA Scitech 2020 Forum*, p. 0814. American Institute of Aeronautics and Astronautics.

WICKERSHAM, P. 2007 Jet mixing enhancement by high amplitude pulse-fluidic actuator. PhD thesis, Georgia Institute of Technology.

WU, Z., FAN, D., ZHOU, Y., LI, R. & NOACK, B.R. 2018a Jet mixing optimization using machine learning control. *Exp. Fluids* **59** (8), 131.

WU, Z., WONG, C.W. & ZHOU, Y. 2018*b* Dual-input/single-output extremum-seeking system for jet control. *AIAA J.* **56** (4), 1463–1471.

WU, Z., ZHOU, Y., CAO, H.L. & LI, W.L. 2016 Closed-loop enhancement of jet mixing with extremum-seeking and physics-based strategies. *Exp. Fluids* **57** (6), 107.

YANG, H. & ZHOU, Y. 2016 Axisymmetric jet manipulated using two unsteady minijets. *J. Fluid Mech.* **808**, 362–396.

YANG, H., ZHOU, Y., SO, R.M.C. & LIU, Y. 2016 Turbulent jet manipulation using two unsteady azimuthally separated radial minijets. *Proc. R. Soc. A: Math., Phys. Eng. Sci.* **472** (2191), 20160417.

YU, J., FAN, D., NOACK, B. & ZHOU, Y. 2021 Genetic-algorithm-based artificial intelligence control of a turbulent boundary layer. *Acta Mechanica Sin.* **37**, 1739–1747.

ZHANG, M.M., CHENG, L. & ZHOU, Y. 2004 Closed-loop-controlled vortex shedding and vibration of a flexibly supported square cylinder under different schemes. *Phys. Fluids* **16** (5), 1439–1448.

ZHOU, Y., DU, C., MI, J. & WANG, X. 2012 Turbulent round jet control using two steady minijets. *AIAA J.* **50**, 736–740.

ZHOU, Y., FAN, D., ZHANG, B., LI, R. & NOACK, B.R. 2020 Artificial intelligence control of a turbulent jet. *J. Fluid Mech.* **897**, A27.